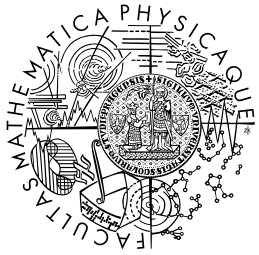

FACULTY
OF MATHEMATICS
AND PHYSICS
Charles University

MASTER THESIS

Bc. Jan Šetina

Optical and magneto-optical spectroscopy of ultrathin films of ferrimagnetic garnets

Institute of Physics of Charles University

Supervisor of the bachelor thesis: RNDr. Martin Veis, Ph.D.
Study programme: Physics
Study branch: Optics and Optoelectronics

Prague 2021

I declare that I carried out this master thesis independently, and only with the cited sources, literature and other professional sources. It has not been used to obtain another or the same degree.

I understand that my work relates to the rights and obligations under the Act No. 121/2000 Sb., the Copyright Act, as amended, in particular the fact that the Charles University has the right to conclude a license agreement on the use of this work as a school work pursuant to Section 60 subsection 1 of the Copyright Act.

In ..... date ....

Author's signature

Thanks to everyone involved...

Title: Optical and magneto-optical spectroscopy of ultrathin films of ferrimagnetic garnets

Author: Bc. Jan Šetina

Institute: Institute of Physics of Charles University

Supervisor: RNDr. Martin Veis, Ph.D., Institute of Physics of Charles University

Abstract: The aim of this master thesis is to prepare and systematically characterize two groups of ultra-thin films of iron garnets with different compositions and deposition conditions. The first set consists of approximately 10 nm thick samples of gallium-doped yttrium-iron garnet on gadolinium gallium garnet ($Gd_3Ga_5O_{12}$) (GGG) substrates with different crystallographic orientations and different annealing temperatures. The second group contains gallium-bismuth-doped neodymium-iron garnet on GGG substrates. These samples have different thicknesses, the concentration of individual elements and different annealing temperatures. All samples were prepared by the metal-organic decomposition method.
The analysis of their physical properties was done by magneto-optical and optical experiments. Specifically, magneto-optical Kerr effect spectroscopy, Faraday hysteresis loops measurements and spectroscopic ellipsometry. Obtained experimental results were further used to deduce the spectral dependence of complete permittivity tensor. Its spectral dependence was than discussed with relation to the electronic structure of investigated materials which helped to select the best deposition conditions and substrate orientation.

Keywords: ferrimagnetic garnets magneto-optical Kerr effect, magneto-optical spectroscopy, metal-organic decomposition

Contents

Introduction

Conventional electronics is reaching its physical limits.[1–3] Because of that, scientists are trying to find some other physical phenomena that would allow transfering and processing information much faster and, in terms of energy, more efficiently. Two main fields of study have developed in several decades. These are *spintronics* and *photonics*.

The main principle of spintronics is that the information is carried/represented using the spin of electrons. Its advantages lie in avoiding Joule's heat that is created in conventional wires by Ohmic losses and much higher operational frequencies as the spin dynamics is quite fast. One of the first working devices using spintronics phenomena are the magnetic hard drives, where it helped to significantly increase the storage capacity.[4]

A completely different approach to transmit information is used in the field of photonics. The information here is converted into light waves which are afterwards propagating via optical fibres or integrated waveguides.

Thanks to the development of integrated lasers, filters, resonators, modulators and photodetectors, scientists have recently managed to get closer to the production of an integrated photonic processor.[5] Also, first computer microprocessors have been developed that communicate between processors and RAM only optically.[6] These microprocessors show a large increase in transfer speed but their functionality is still very limited. One of the very important things for a photonic chip to work properly is to suppress back reflections from integrated optical components. They are caused by imperfections made during the lithographic process. Practically, magneto-optical (MO) insulators (optical unidirectional devices using non-reciprocal light propagation in magneto-optical material) are commonly used. However, their integration on an optical chip is very complicated due to the incompatibility of classic magneto-optical materials with silicon technology.

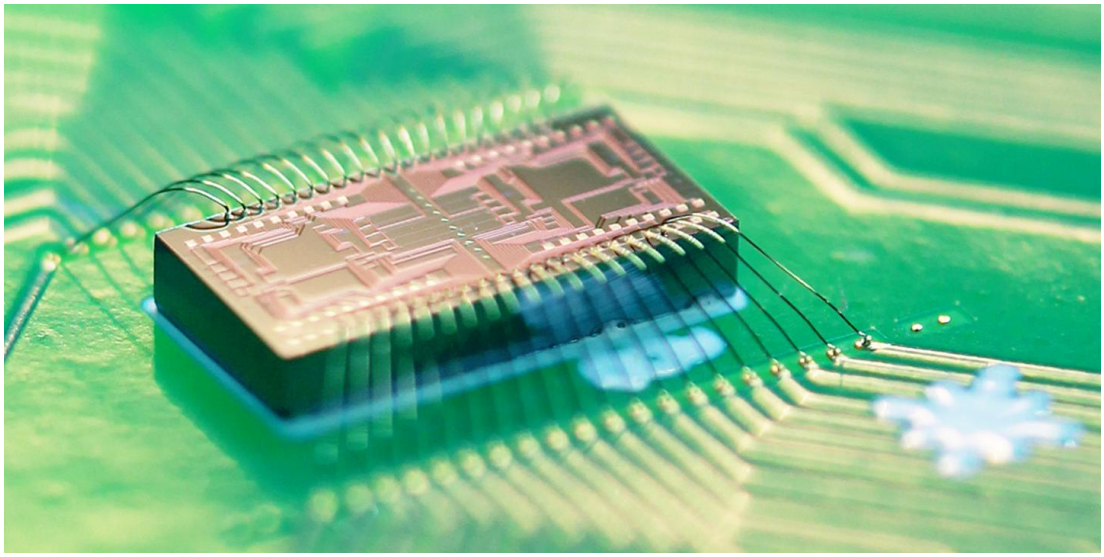

Figure 1: A multi-component photonic integrated circuit.[7]

Conventional magneto-optical materials (magnetic garnet structures) in the form of thin layers deposited on a silicon substrate do not show magneto-optical

properties required for a functional integrated magneto-optical element. Recently, experiments using the deposition of garnet layers on a silicon substrate using special substrates or post-deposition annealing were performed. [8, 9] This led to the possibility of demonstrating the first integrated magneto-optical insulating element.[10] However, its properties are very limited and such a concept is not very suitable for application purposes. The subject of interest of several renowned world laboratories dealing with this issue is therefore to find suitable materials and methods for the preparation of thin films that ensure the optical and magneto-optical response of deposited layers similar to bulk crystals that are commonly used.

One of the suitable candidates of materials is a group of the ferrimagnetic iron garnets with general formula $X_3Fe_5O_{12}$, where X stands for any element of the 3b groups of the periodic table of elements or a rare earth element. The basic crystallographic structure of the garnets is formed by a cubic elementary cell in which there are 3 sublattices formed by oxygen atoms: dodecahedral (occupied by three X ions), octahedral (occupied by two iron ions) and tetrahedral (occupied by three iron ions). The most well-known representative, which has been widely researched for several decades, but still does not lose popularity due to its unrivalled magnetic properties, is the yttrium iron garnet $Y_3Fe_5O_{12}$ (YIG). In addition, by substituting yttrium atoms for other elements such as Tb, Tm, Eu, Bi, Nd, etc., it is possible to change the magnetic, optical and magneto-optical properties. These properties can also be altered by the partial replacement of iron atoms. For example, it turns out that with different iron ratios in individual sublattices, the compensation temperature of these materials changes.[11]

The theme of this work is the characterization of two groups of ultra-thin films of ferrimagnetic garnets. In the first group there are four samples of $Y_3Fe_4Ga_1O_{12}$ on $Gd_3Ga_5O_{12}$ substrates with different orientations and different annealing temperatures. The aim is to describe how annealing temperature changes the electronic structure and how the orientation of the substrate changes the magneto-optical properties of the thin films. The second group of samples consists of nine samples of $Nd_xBi_{3-x}Fe_4Ga_1O_{12}$ on $Gd_3Ga_5O_{12}$ (100) substrates with different annealing temperatures, thicknesses and concentrations of individual ions. The aim here is to describe how the temperature changes the electronic structure and how the thickness of the material changes its magnetic properties. This will help to select the best preparation conditions.

This thesis is organized into three parts. The introductory part contains the theoretical background consisting of the general description of light, matter and the interaction between them. In the second part, there is a description of experimental methods used in this thesis and the general information about ferrimagnetic garnets and their preparation method. The third then part contains the results of studied materials.

Part I

Theoretical background

This thesis is focused on the optical and magneto-optical properties of ferrimagnetic garnets. Several experimental techniques that utilize light are used to measure these properties. For many methods, like spectroscopy, it is convenient to use wave description of light together with Jones formalism.

This part, therefore, summarizes the fundamentals basics of the electromagnetic theory of light, which is necessary for this work, and provides a description of the matter in general with emphasis on ferrimagnetic garnets.

1. Description of light

1.1 Wave equation

The electromagnetic wave equation is derived from Maxwell's equations using constitutive relations and Ohm's law. Maxwell's equations are universal equations that link together vectors of electric field $\boldsymbol{E}$, magnetic induction $\boldsymbol{B}$, electric induction (displacement field) $\boldsymbol{D}$, magnetic field strength $\boldsymbol{H}$, free current density $\boldsymbol{j}$ and free charge density ρ. Using SI units and the differential form, macroscopic Maxwell's equations are as follows:

$$\nabla \times \boldsymbol{E} + \frac{\partial \boldsymbol{B}}{\partial t} = 0\,, \tag{1.1a}$$

$$\nabla \cdot \boldsymbol{B} = 0\,, \tag{1.1b}$$

$$\nabla \times \boldsymbol{H} - \frac{\partial \boldsymbol{D}}{\partial t} = \boldsymbol{j}\,, \tag{1.1c}$$

$$\nabla \cdot \boldsymbol{D} = \rho\,. \tag{1.1d}$$

This set of equations are valid for all materials. However, for the purpose of this thesis we will now restrict ourselves to systems (isotropic, static medium ($\frac{\partial \boldsymbol{\mu}}{\partial t}, \frac{\partial \boldsymbol{\varepsilon}}{\partial t}, \frac{\partial \boldsymbol{\sigma}}{\partial t} = \boldsymbol{0}$)) that obey following relations known as constitutive relations:

$$\boldsymbol{B} = \boldsymbol{\mu}\boldsymbol{H}\,, \tag{1.2a}$$

$$\boldsymbol{D} = \boldsymbol{\varepsilon}\boldsymbol{E}\,, \tag{1.2b}$$

$$\boldsymbol{j} = \boldsymbol{\sigma}\boldsymbol{E}\,. \tag{1.2c}$$

We denote $\boldsymbol{\mu} = \mu_0\mu_r$ and $\boldsymbol{\varepsilon} = \varepsilon_0\varepsilon_r$ as tensors of relative permeability and permittivity; μ_0 and ε_0 as permeability and permittivity of vacuum; μ_r and ε_r as relative permeability and permittivity. $\boldsymbol{\sigma}$ then represents the conductivity tensor, making the last equation equivalent to Ohm's law.

Inserting equation (1.2a) into (1.1a) and (1.2b) with (1.2c) into (1.1c) and their further adjustments gives us following equations:

$$\nabla \times (\frac{1}{\boldsymbol{\mu}}\nabla \times \boldsymbol{E}) + \nabla \times \frac{\partial \boldsymbol{H}}{\partial t} = 0\,, \tag{1.3a}$$

$$\nabla \times \frac{\partial \boldsymbol{H}}{\partial t} - \boldsymbol{\varepsilon}\frac{\partial^2 \boldsymbol{E}}{\partial t^2} - \boldsymbol{\sigma}\frac{\partial E}{\partial t} = 0\,. \tag{1.3b}$$

By substituting (1.3b) into (1.3a) and using identity $\nabla \times \nabla = \nabla\nabla - \Delta$ we have second-order partial differential equation with respect to E

$$\Delta \boldsymbol{E} - \boldsymbol{\mu}\boldsymbol{\varepsilon}\frac{\partial^2 \boldsymbol{E}}{\partial t^2} - \boldsymbol{\mu}\boldsymbol{\sigma}\frac{\partial \boldsymbol{E}}{\partial t} + \nabla \ln \boldsymbol{\mu} \times (\nabla \times \boldsymbol{E}) - \nabla(\nabla \cdot \boldsymbol{E}) = 0\,. \tag{1.4}$$

It is the most general form of electromagnetic wave equation.

However, the wave equation (1.4) can be simplified by further assumptions:

(a) environment without charges $\cdots \rho = 0$

$$\Delta \boldsymbol{E} - \boldsymbol{\mu\varepsilon}\frac{\partial^2 \boldsymbol{E}}{\partial t^2} - \boldsymbol{\mu\sigma}\frac{\partial \boldsymbol{E}}{\partial t} + \nabla \ln \boldsymbol{\mu} \times (\nabla \times \boldsymbol{E}) - \nabla(\boldsymbol{E} \cdot \nabla \ln \boldsymbol{\varepsilon}) = 0 \quad (1.5)$$

(b) homogeneous environment $\cdots \boldsymbol{\mu} = const.$, $\boldsymbol{\varepsilon} = const.$

$$\Delta \boldsymbol{E} - \boldsymbol{\mu\varepsilon}\frac{\partial^2 \boldsymbol{E}}{\partial t^2} - \boldsymbol{\mu\sigma}\frac{\partial \boldsymbol{E}}{\partial t} = 0 \quad (1.6)$$

(c) non-conductive environment $\cdots \boldsymbol{\sigma} = 0$

$$\Delta \boldsymbol{E} - \boldsymbol{\mu\varepsilon}\frac{\partial^2 \boldsymbol{E}}{\partial t^2} = 0 \quad (1.7)$$

1.1.1 Plane wave solution in vacuum

Suppose vacuum, equation (1.7) can be rewritten to the most known form of the wave equation

$$\Delta \boldsymbol{E} - \frac{1}{c^2}\frac{\partial^2 \boldsymbol{E}}{\partial t^2} = 0\,, \quad (1.8)$$

where $c = 1/\sqrt{\mu_0 \varepsilon_0}$ is the speed of light in vacuum.

Basic solution to this wave equation can be given in a form of a plane wave. A plane wave represents any solution of the equation (1.8) in the form $\mathbf{E}(\boldsymbol{r}, t) = \boldsymbol{E}(\boldsymbol{r} \cdot \boldsymbol{s}, t)$, where $\boldsymbol{s}$ is a unit vector in the direction of motion of the wave and $\boldsymbol{r}$ is a position vector of one of the points on the wave plane. It can be written as:

$$\boldsymbol{E}(\boldsymbol{r}, t) = \boldsymbol{E}_0 \cos(\omega t - \boldsymbol{k} \cdot \boldsymbol{r} + \delta) = \mathrm{Re}\{\boldsymbol{E}_0 e^{i(\omega t - \boldsymbol{k}\cdot\boldsymbol{r} + \delta)}\}\,, \quad (1.9)$$

where $\boldsymbol{E}_0$ is the amplitude of the wave, ω is the angular frequency, $\boldsymbol{k}$ is the wave vector and δ is the initial phase shift. Wave vector $\boldsymbol{k}$ is defined as

$$\boldsymbol{k} = \boldsymbol{s} \cdot \frac{\omega}{c}. \quad (1.10)$$

From this form, the wave vector in vacuum can be derived as

$$\boldsymbol{k}_0 = \boldsymbol{s} \cdot \frac{\omega}{c_0} \quad (1.11)$$

by using refractive index through definition

$$n = \frac{c_0}{c}\,, \quad (1.12)$$

where c_0 is the speed of light in vacuum and c is the phase velocity of light in the medium. Inserting (1.11) into (1.9) provides different form of solution of wave equation:

$$\boldsymbol{E}(\boldsymbol{r}, t) = \mathrm{Re}\Big\{\boldsymbol{E}_0 e^{i(\omega t - n\boldsymbol{k}_0 \cdot \boldsymbol{r} + \delta)}\Big\}. \quad (1.13)$$

By inserting this solution to Maxwell's equations (1.1), following equations can be derived:

$$\boldsymbol{k} \cdot \boldsymbol{E} = 0\,, \quad (1.14)$$

$$\boldsymbol{k} \cdot \boldsymbol{B} = 0\,, \quad (1.15)$$

$$\boldsymbol{s} \times \boldsymbol{E} = c\boldsymbol{B}\,. \quad (1.16)$$

This relations shows that vectors $\boldsymbol{E}$, $\boldsymbol{B}$ and $\boldsymbol{s}$ form orthogonal system. It means that every electromagnetic plane wave is always transversal. The equation (1.16) can provide another formula

$$E_0 = cB_0\,, \tag{1.17}$$

which binds the amplitudes of the electric and the magnetic part of the wave. Schematic representation of electromagnetic wave is shown in fig. 1.1.

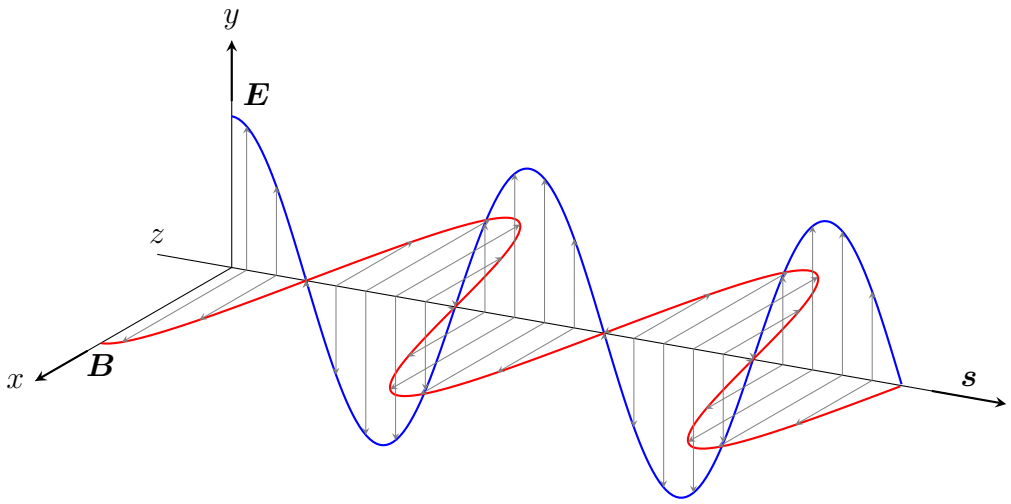

Figure 1.1: Linearly polarized electromagnetic wave propagating in the direction +z.

1.2 Polarization

Due to the fact that magneto-optical measurements utilize polarized light, it is appropriate to describe the polarization of light.

Polarization is a general property of every vectorial wave, such as an electromagnetic wave. It describe the geometrical oscillations of electric vector $\boldsymbol{E}$; because $\boldsymbol{E}$ is dominating in the interaction of light with matter (see (1.17)). Further in this section, we will work with electromagnetic waves described by equation (1.13) which propagate along the z axis.

Let there be two time-harmonic monochromatic plane waves of the same frequency. Also, let the oscillations of one wave be parallel to the x axis and the other wave parallel to the y axis. Superposition of two waves in terms of its components is as follows:

$$E_x(z,t) = E_{0x}\,\cos(\omega t - kz + \delta_x)\,, \tag{1.18}$$

$$E_y(z,t) = E_{0y}\,\cos(\omega t - kz + \delta_y)\,, \tag{1.19}$$

$$E_z(z,t) = 0\,, \tag{1.20}$$

where E_{0x}, E_{0y} are amplitudes of each component, δ_x, δ_y are their phases, ω is angular frequency and k is the magnitude of the wavevector.

Then, $\tau \coloneqq (\omega t - kz)$ can be defined; if equations (1.18) and (1.19) are divided by their respective amplitudes, one can obtain

$$\frac{E_x}{E_{0x}} = \cos(\tau + \delta_x) = \cos(\tau)\cos(\delta_x) - \sin(\tau)\sin(\delta_x)\,, \tag{1.21}$$

$$\frac{E_y}{E_{0y}} = \cos(\tau + \delta_y) = \cos(\tau)\cos(\delta_y) - \sin(\tau)\sin(\delta_y)\,. \tag{1.22}$$

Let multiply (1.21), (1.22) by $\sin\delta_y$, $\sin\delta_x$, respectively, and subtract them. Similarly, multiply the same equations by $\cos\delta_y$, $\cos\delta_x$ and subtract them. Thereafter, following equations are acquired:

$$\frac{E_x}{E_{0x}}\sin\delta_y - \frac{E_y}{E_{0y}}\sin\delta_x = \cos(\tau)\sin(\delta_y - \delta_x)\,, \tag{1.23}$$

$$\frac{E_x}{E_{0x}}\cos\delta_y - \frac{E_y}{E_{0y}}\cos\delta_x = \sin(\tau)\sin(\delta_y - \delta_x)\,. \tag{1.24}$$

Now, let square and sum (1.23) and (1.24). With the definition of δ ($\delta \coloneqq \delta_y - \delta_x$), subsequent formula is attained:

$$\left(\frac{E_x}{E_{0x}}\right)^2 - 2\frac{E_x}{E_{0x}}\frac{E_y}{E_{0y}}\cos\delta + \left(\frac{E_y}{E_{0y}}\right)^2 = \sin^2\delta\,. \tag{1.25}$$

The equation above is a formula for an ellipse. That means that, in general, the endpoint of electric field vector $\boldsymbol{E}$ is tracing the shape of an ellipse in projection on the plane perpendicular to the direction of propagation z (see figure 1.2). This ellipse, which describes the polarization state of light, can be fully characterized by four parameters:

- the overall *amplitude* E_0 – can be calculated as $E_0 = \sqrt{a^2 + b^2}$ and relates to the intensity of light as $I = E_0^2$
- the *azimuth* Ψ – an oriented angle between the semi-major axis a and the positive half-axis x, $\Psi \in [-\frac{\pi}{2}; \frac{\pi}{2}]$
- the *ellipticity* angle ε – an angle that satisfies the equation $\tan\varepsilon = \mp\frac{b}{a}$, $\varepsilon \in [-\frac{\pi}{2}; \frac{\pi}{2}]$
- the *absolute phase* δ_0 – angle between vector $\boldsymbol{E}$ in time $t = 0$ and the positive half-axis x, provides information about the initial state of the wave, $\delta_0 \in [-\pi; \pi]$

The ellipticity $e = \tan\varepsilon$ can take values from -1 to 1. Its sign contains information about the direction in which the wave rotates. By convention, positive values mean right-hand polarization and negative values mean left-hand polarization. Zero value then corresponds to linearly polarized light in which electric field vector oscillates only in the so-called plane of polarization, which does not change while propagating through the isotropic medium. If one looks against the direction of propagation, right-handed polarization denotes a clockwise motion of electric field vector whereas the left-hand polarization represents a counterclockwise motion of electric field vector.

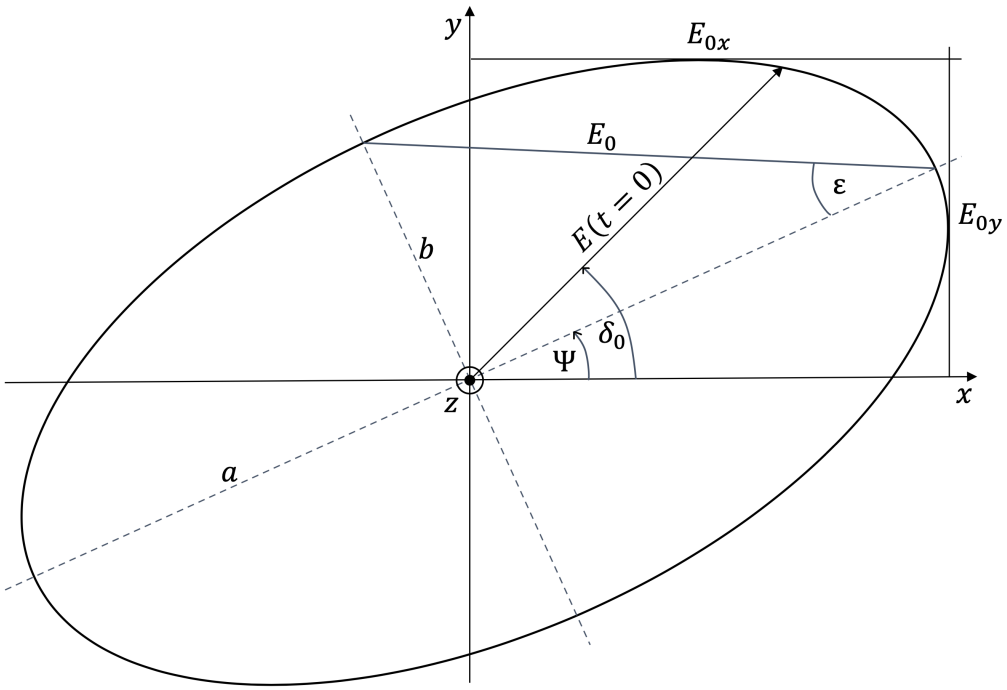

Figure 1.2: Polarization ellipse when looking against the direction of propagation of the light wave. The depicted parameters are semi-major axes a and b, amplitudes E_0x and E_0y, azimuth Ψ, ellipticity ε and absolute phase δ_0.

In some cases, elliptical polarization reduces to circular polarization. That happens for $\varepsilon = \pm\pi/2$. Circularly polarized light then forms in space a symmetrical helix that can be either right or left-handed.

A large number of different formalisms have been developed to simplify the description of polarized light. The most commonly used is the formalism of Jones vectors and matrices. However, its disadvantage is that it can only be used to describe completely polarized light.

1.3 Jones formalism

This section is dedicated to Jones formalism, which is used for the description of the optical system and propagation of linearly polarized light through it.

Jones vector

A plane electromagnetic wave can be written in the symbolism of complex numbers as

$$\boldsymbol{E}(z,t) = E_x\boldsymbol{x} + E_y\boldsymbol{y}, \tag{1.26}$$

where

$$E_x(z,t) = \mathrm{Re}\{E_{0x}e^{i(\omega t - kz + \delta_x)}\} = Re\{A_x e^{i(\omega t - kz)}\}\,, \tag{1.27a}$$

$$E_y(z,t) = \mathrm{Re}\{E_{0y}e^{i(\omega t - kz + \delta_y)}\} = Re\{A_y e^{i(\omega t - kz)}\}\,. \tag{1.27b}$$

Terms A_x, A_y are the complex amplitudes of a monochromatic plane wave, E_{0x}, E_{0y} are the corresponding parts of amplitudes and δ_x, δ_y are the initial phases

of each component of wave. This allows to define Jones vector of polarization $\boldsymbol{J}$ of the light wave propagating in the direction parallel to z axis:

$$\boldsymbol{J} = \begin{bmatrix} E_{0x}e^{i\delta_x} \\ E_{0y}e^{i\delta_y} \end{bmatrix} = \begin{bmatrix} A_x \\ A_y \end{bmatrix} . \tag{1.28}$$

This vector carries the complete information about the polarization state of the wave. The vector (1.28) is defined in the Cartesian basis of linear polarizations. Another important basis is the circular polarization basis consisting of left circular polarization (LCP) and right circular polarization (RCP). Both bases can be found below.

- The Cartesian basis:

$$\boldsymbol{J}_x = \begin{bmatrix} 1 \\ 0 \end{bmatrix} , \ \boldsymbol{J}_y = \begin{bmatrix} 0 \\ 1 \end{bmatrix} \tag{1.29}$$

- The circular basis:

$$\boldsymbol{J}_L = \frac{1}{\sqrt{2}} \begin{bmatrix} 1 \\ -i \end{bmatrix} , \ \boldsymbol{J}_R = \frac{1}{\sqrt{2}} \begin{bmatrix} 1 \\ i \end{bmatrix} \tag{1.30}$$

Sometimes, it is useful to rotate the whole Cartesian system by angle θ. ($\theta > 0$ if the rotation is in the counterclockwise direction.). The rotation matrix is as follows

$$\boldsymbol{R}(\theta) = \begin{bmatrix} \cos\theta & -\sin\theta \\ \sin\theta & \cos\theta \end{bmatrix} . \tag{1.31}$$

General elliptical polarization with a specific Ψ and ϵ is achieved by the following procedure. Considering an ellipse with the azimuth equal to zero ($\Psi = 0$) and arbitrary ellipticity angle ϵ. Then let rotate the Cartesian system clockwise by the azimuth Ψ (i.e. rotation of the ellipse counterclockwise) with use of (1.31). Jones vector for general polarization is then

$$\boldsymbol{J}_{XY} = \begin{bmatrix} \cos\theta & -\sin\theta \\ \sin\theta & \cos\theta \end{bmatrix} \begin{bmatrix} \cos\epsilon \\ i\sin\epsilon \end{bmatrix} = \begin{bmatrix} \cos\theta\cos\epsilon - i\sin\theta\sin\epsilon \\ \sin\theta\cos\epsilon + i\cos\theta\sin\epsilon \end{bmatrix} . \tag{1.32}$$

Further, if one is neither interested in intensity nor an absolute phase of the wave, *complex polarization parameter* χ, which also describe polarization state, can be defined as a ration of the second to the first component of the Jones vector (1.28) [12]

$$\chi = \tan\alpha \, e^{i\delta} . \tag{1.33}$$

Absolute value and the argument are

$$|\chi| = \tan\alpha = \frac{A_y}{A_x} , \tag{1.34}$$

$$\arg(\chi) = \delta_y - \delta_x = \delta . \tag{1.35}$$

Newly defined parameters are related to previously introduced parameters Ψ and ϵ through relations [13]

$$\tan 2\Psi = \tan 2\alpha \cos\delta , \tag{1.36a}$$

$$\sin 2\epsilon = \sin 2\alpha \sin\delta . \tag{1.36b}$$

Using parameters α and δ, Jones vector can be then rewritten as

$$\boldsymbol{J} = \begin{bmatrix} \cos\alpha \\ \sin\alpha \; e^{i\delta} \end{bmatrix} . \tag{1.37}$$

In this approach each polarization state is represented by one point in the complex plane, therefore the complex polarization parameter is related to the Cartesian basis.

The complex parameter χ of an arbitrary elliptical polarization (with respect to the Cartesian basis) can be defined using (1.32) as

$$\chi = \frac{\sin\Psi\cos\epsilon + i\cos\Psi\sin\epsilon}{\cos\Psi\cos\epsilon - i\sin\Psi\sin\epsilon} = \frac{\tan\Psi + i\tan\epsilon}{1 - i\tan\Psi\tan\epsilon} . \tag{1.38}$$

Provided that the angles Ψ and ϵ are very small, an approximation of the tangent function by its argument can be made (first terms of Taylor series: $\tan\Psi \approx \Psi$, $\tan\epsilon \approx \epsilon$). If one neglect also the second-order term in the denominator, (1.38) can be then simplifiedd as

$$\chi \approx \Psi + i\epsilon . \tag{1.39}$$

Jones matrix

Jones formalism can very well describe the interaction of a light wave with an optical element which leads to the change of polarization state of the wave.

Assume light wave propagating against optical element described by reflection matrix $\boldsymbol{R}_{sp}$, which is expressed in terms of *s*- and *p*- polarization. Cartesian coordinates are such that direction of the x axis is perpendicular to the plane of incidence, light polarized linearly in this direction is called *s*-polarized. y axis is then parallel with the plane of incidence, light polarized linearly in this direction is called *p*-polarized. Axis z is defined such that it is always in the direction of propagation of the light wave (as seen in figure 1.3a). Also, suppose that the incident wave is described by Jones vector $\boldsymbol{J}^{(I)}$ and the reflected wave by $\boldsymbol{J}^{(R)}$. The relation between these two states can be written as

$$\boldsymbol{J}^{(R)} = \boldsymbol{R}_{sp}\,\boldsymbol{J}^{(I)} , \tag{1.40}$$

where $\boldsymbol{R}_{sp}$ is the Jones reflection matrix

$$\boldsymbol{R}_{sp} = \begin{bmatrix} r_{ss} & r_{sp} \\ r_{ps} & r_{pp} \end{bmatrix} . \tag{1.41}$$

Coefficients r_{ss}, r_{sp}, r_{ps}, r_{pp} are amplitude reflection coefficients for *s*- and *p*- polarized light waves. For an isotropic material, which is not located in a magnetic field, the matrix (1.41) is diagonal, i.e. there is no interaction between *s*- and *p*- polarized waves. However, upon insertion of the material into a magnetic field that induces optical anisotropy, the non-diagonal elements generally become non-zero, which corresponds to the interaction of *s*- and *p*- polarized waves.

Above mentioned amplitude reflection coefficients can be written with use of equations (1.28), (1.40) and denotation of complex amplitudes of both incident

and reflected wave $A_x = A_s$ and $A_y = A_p$ as

$$r_{ss} = \left(\frac{A_s^{(R)}}{A_s^{(I)}} \right)_{A_p^{(I)}=0} , \tag{1.42a}$$

$$r_{sp} = \left(\frac{A_s^{(R)}}{A_p^{(I)}} \right)_{A_s^{(I)}=0} , \tag{1.42b}$$

$$r_{ps} = \left(\frac{A_p^{(R)}}{A_s^{(I)}} \right)_{A_p^{(I)}=0} , \tag{1.42c}$$

$$r_{pp} = \left(\frac{A_p^{(R)}}{A_p^{(I)}} \right)_{A_s^{(I)}=0} . \tag{1.42d}$$

r_{sp}, r_{ps} then represent the conversion of one polarization state to the other and r_{ss}, r_{pp} represent Fresnel reflection coefficients.

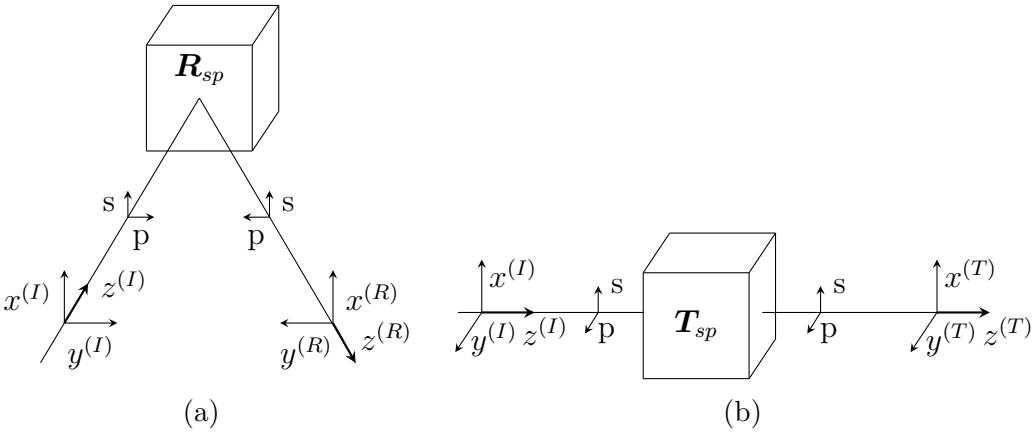

Figure 1.3: Cartesian coordinate systems for reflection optical element characterized by Jones refection matrix $\boldsymbol{R}_{sp}$ (a) and transmission optical element characterized by Jones transmission matrix $\boldsymbol{T}_{sp}$.

Similarly, all information above also applies to a system, where light is propagating through an optical element, which is described by transmission matrix $\boldsymbol{T}_{sp}$. Arrangement of such system along with previously defined Cartesian system as well as *s*-, *p*- polarizations can be seen in figure 1.3b. The relation between incident wave ($\boldsymbol{J}^{(I)}$) and transmitted wave ($\boldsymbol{J}^{(T)}$) can be then written as

$$\boldsymbol{J}^{(T)} = \boldsymbol{T}_{sp}\, \boldsymbol{J}^{(I)} , \tag{1.43}$$

where Jones transmission matrix $\boldsymbol{T}_{sp}$ is defined as

$$\boldsymbol{T}_{sp} = \begin{bmatrix} t_{ss} & t_{sp} \\ t_{ps} & t_{pp} \end{bmatrix} . \tag{1.44}$$

Amplitude reflection coefficients t_{ss}, t_{sp}, t_{ps}, t_{pp} can be written analogously to

(1.42a)–(1.42d) as

$$t_{ss} = \left(\frac{A_s^{(T)}}{A_s^{(I)}} \right)_{A_p^{(I)}=0}, \tag{1.45a}$$

$$t_{sp} = \left(\frac{A_s^{(T)}}{A_p^{(I)}} \right)_{A_s^{(I)}=0}, \tag{1.45b}$$

$$t_{ps} = \left(\frac{A_p^{(T)}}{A_s^{(I)}} \right)_{A_p^{(I)}=0}, \tag{1.45c}$$

$$t_{pp} = \left(\frac{A_p^{(T)}}{A_p^{(I)}} \right)_{A_s^{(I)}=0}. \tag{1.45d}$$

The optical system usually does not consist of only one optical element. Each optical element is described by reflection/transmission matrix $\boldsymbol{M}_n$, which can be then consecutively multiplied to form final matrix $\boldsymbol{M}$

$$\boldsymbol{M} = \boldsymbol{M}_n \dots \boldsymbol{M}_1 . \tag{1.46}$$

The resulting matrix works the same way as in equation (1.40) or (1.43).

At the end of this section, matrices for basic optical elements are listed below.

Cartesian basis **Circular basis**

linear polarizer oriented at angle ϕ with respect to x axis:

$$\boldsymbol{P}_{cart} = \begin{bmatrix} \cos^2\varphi & \sin\varphi\cos\varphi \\ \sin\varphi\cos\varphi & \sin^2\varphi \end{bmatrix} \tag{1.47}$$

$$\boldsymbol{P}_{circ} = \frac{1}{\sqrt{2}} \begin{bmatrix} 1 & e^{2i\varphi} \\ e^{-2i\varphi} & 1 \end{bmatrix} \tag{1.48}$$

phase plate with with retardance of Γ witch principal axis parallel to x and y:

$$\boldsymbol{C}_{cart} = \begin{bmatrix} e^{i\Gamma/2} & 0 \\ 0 & e^{-i\Gamma/2} \end{bmatrix} \tag{1.49}$$

$$\boldsymbol{C}_{circ} = \begin{bmatrix} \cos\frac{\Gamma}{2} & i\sin\frac{\Gamma}{2} \\ i\sin\frac{\Gamma}{2} & \cos\frac{\Gamma}{2} \end{bmatrix} \tag{1.50}$$

polarization rotator, which rotates the polarization plane by an angle θ:

$$\boldsymbol{T}_{cart} = \begin{bmatrix} \cos\theta & -\sin\theta \\ \sin\theta & \cos\theta \end{bmatrix} \tag{1.51}$$

$$\boldsymbol{T}_{circ} = \begin{bmatrix} e^{i\theta} & 0 \\ 0 & e^{-i\theta} \end{bmatrix} \tag{1.52}$$

1.4 Magneto-optical effects

When light wave reflects or passes through a sample placed in a magnetic field, the polarization state of the light wave will change. That effect is described by so-called *magneto-optical observables*. The case of reflection is then called the magneto-optical Kerr effect (MOKE) and the case of transmission is called the magneto-optical Faraday effect.

Let the incident wave be (s-polarized) and let it reflects off the material in a magnetic field (i.e. magnetized material). Then the reflected beam is described by Jones vector $\begin{bmatrix} r_{ss} \\ r_{ps} \end{bmatrix}$. Also let the angles $\Psi_s^{(R)}$ and $\epsilon_s^{(R)}$ be small to satisfy equation (1.39). Jones reflection matrix of the material is no longer diagonal and therefore the ratio of the off-diagonal to diagonal elements of the matrix (1.41) (in this case transformation of the incident s-polarized light wave (1.42a) to a reflected p-polarized light wave (1.42c)) can be expressed as

$$\frac{r_{ps}}{r_{ss}} = \left(\frac{\frac{A_p^{(R)}}{A_s^{(I)}}}{\frac{A_s^{(R)}}{A_s^{(I)}}} \right)_{A_p^{(I)}=0} = \left(\frac{A_p^{(R)}}{A_s^{(R)}} \right)_{A_p^{(I)}=0} = \chi_s^{(R)} \,. \tag{1.53}$$

Complex quantity Kerr angle Φ_{Ks}, which describes MOKE, can be defined for polar configuration as [12]

$$-\frac{r_{ps}}{r_{ss}} =: \Phi_{Ks} \approx \Psi_{Ks} - i\,\epsilon_{Ks} \tag{1.54}$$

where Ψ_{Ks} is *Kerr rotation* that describe rotation of polarization plane and ϵ_{Ks} is *Kerr ellipticity* which describes the change in ellipticity of a polarization ellipse.

The derivation for the case of an incident p-polarized wave is done analogously. Using (1.42b) and (1.42d) one can obtain

$$\frac{r_{sp}}{r_{pp}} = \left(\frac{\frac{A_s^{(R)}}{A_p^{(I)}}}{\frac{A_p^{(R)}}{A_p^{(I)}}} \right)_{A_s^{(I)}=0} = \left(\frac{A_s^{(R)}}{A_p^{(R)}} \right)_{A_s^{(I)}=0} = (\chi_p^{(R)})^{-1} \,. \tag{1.55}$$

Since the fraction of the off-diagonal and diagonal element is usually small, one can derive the magneto-optical Kerr angle for an incident p-polarized wave as

$$\frac{r_{sp}}{r_{pp}} =: \Phi_{Kp} \approx \Psi_{Kp} - i\,\epsilon_{Kp} \tag{1.56}$$

In similar way *Faraday rotation* Ψ_F and *Faraday ellipticity* (*magnetic circular dichroism* (MCD)[1]) ϵ_F for s- and p- polarization can be defined with use of (1.45a)–(1.45d) as

$$-\frac{t_{ps}}{t_{ss}} =: \Phi_{Fs} \approx \Psi_{Fs} - i\,\epsilon_{Fs} \tag{1.57a}$$

$$\frac{t_{sp}}{t_{pp}} =: \Phi_{Fp} \approx \Psi_{Fp} - i\,\epsilon_{Fp} \tag{1.57b}$$

[1]Faraday ellipticity = magnetic circular dichroism (MCD)

Should the angle of incidence is zero, following relations, based on the symmetry of the problem (switching basis upon reflection (see figure 1.3a)), must be fullfiled

$$-r_{ss} = r_{pp}\,, \tag{1.58a}$$

$$r_{sp} = r_{ps}\,. \tag{1.58b}$$

For normal light incidence further apply

$$\Phi_{Ks} = \Phi_{Kp} = \Phi_K\,, \tag{1.59a}$$

$$\Phi_{Fs} = \Phi_{Fp} = \Phi_F\,. \tag{1.59b}$$

For more detailed approach see [12].

2. Description of matter

2.1 Ferrimagnetism

The origin of magnetism is in the exchange interaction between atoms. More precisely it is determined by the magnetic dipole moment of the atom, which comes from the orbital angular momentum and the spin (angular momentum) of electrons.[1]

Magnetic materials are divided into five basic types of magnetism: ferromagnetism, antiferromagnetism, ferrimagnetism, paramagnetism and diamagnetism. Three of them are shown in figure 2.1. The divisions are based on the response of the material to the external magnetic field. Because investigated materials in this work are ferrimagnetic garnets, the further text will focus only on materials with ferrimagnetic order.

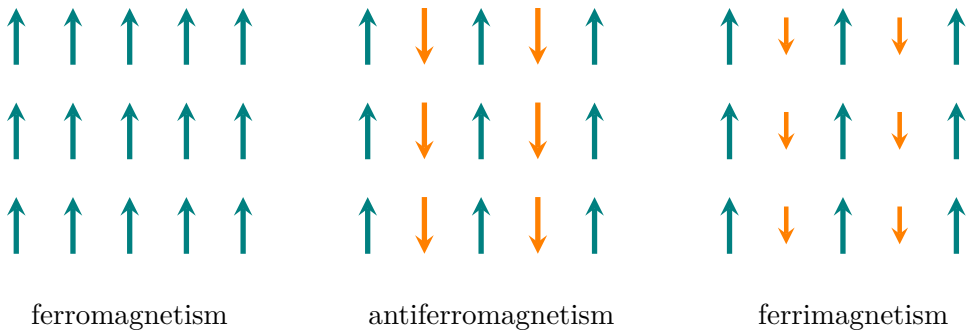

Figure 2.1: Scheme of different types of magnetic ordering in magnetic material.

Ferrimagnets are materials with two or more magnetic sublattices whose magnetic moments are generally oppositely oriented. Ordinarily, such a substance shows spontaneous net magnetization[2] ($M_S \approx 150$ kA/m[3]) that is usually much smaller than in the case of ferromagnets ($M_S \approx 500 - 1500$ kA/m [15, 16]). [17] This magnetic alignment occurs in materials that consist of at least two different atoms or ions. Their unpaired valence electrons interacts with each other inducing strong parallel or antiparallel alignments. Most often they are compounds of metals and oxides; e.g. ferrites containing Fe^{3+} and Fe^{2+} in various sublattices. [17]

The best-known representative is Fe_3O_4. In this material, three iron ions (two Fe^{3+} ions and one Fe^{2+} ion) belong to four ions of oxygen. Magnetic moments of the two Fe^{3+} ions are oriented in the opposite directions and therefore do not participate in the formation of an external magnetic moment. Thus, only the last remaining iron ion contributes to the resulting external magnetic field. Other representatives may include yttrium–iron garnets $Y_3Fe_5O_{12}$ (YIG), $PbFe_{12}O_{19}$, $BaFe_{12}O_{19}$, as well as iron and sulfur compounds ($Fe_{1-x}S$). [18]

[1] Some other mechanisms contribute to the magnetic dipole moment of the atom like the angular momentum of a nucleus. However, the efects of these mechanisms are small and therefore, for the purpose of this work, can be neglected.

[2] unlike antiferromagnets

[3] the magnetic dipole moment per unit volume of material [14]

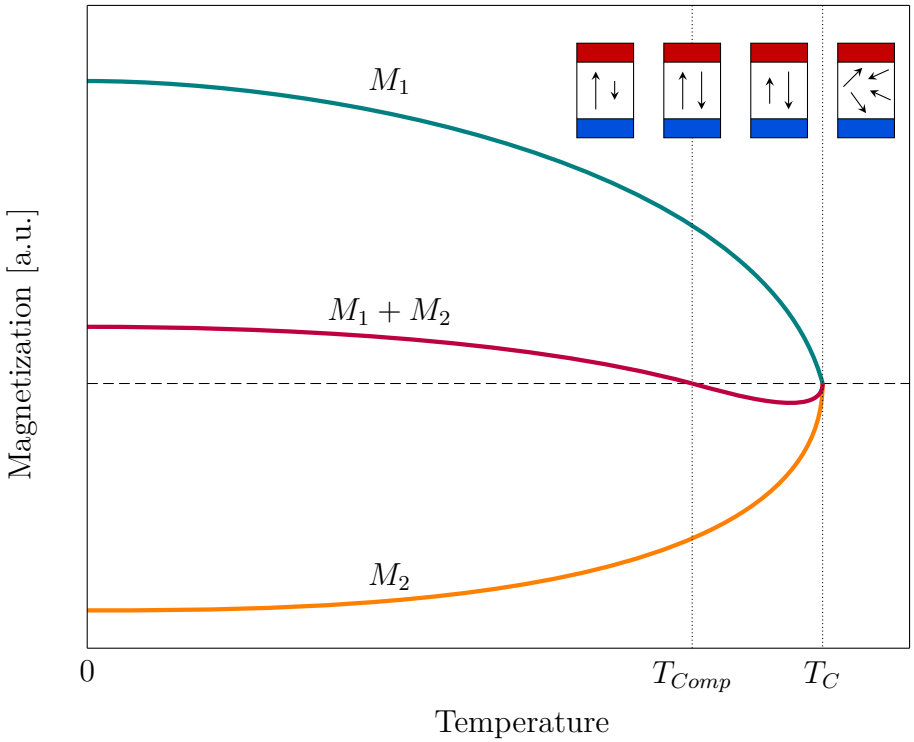

Figure 2.2: Dependence of magnetization of ferrimagnet on temperature. M_1 and M_2 stand for contribution of individual magnetic sublattices, $M_1 + M_2$ is the resulting net magnetization. T_{Comp} is compensation temperature and T_C is Curie temperature.

2.1.1 Critical temperature

Ferrimagnets have very similar magnetic properties to ferromagnets – they show spontaneous magnetization below the critical (so-called *Curie*) temperature (which is different for each material), and at a temperature higher than the mentioned critical value, the materials become magnetically disordered (paramagnetic) (see figure 2.2). This is due to the fact that the hitherto properly arranged magnetic moments of the individual atoms become chaotic due to thermal excitations, and thus the magnetic moment of the individual atoms is compensated by other atoms. [18]

2.1.2 Compensation temperature

The magnetic moment of each magnetic sublattice lowers with increasing temperature. However, each of them has different temperature dependance. Hence another specific temperature can by defined – *compensation temperature*. When the temperature of the material reaches this value, oppositely aligned magnetic moments are the same size (see figure 2.2) and the net magnetic moment vanishes. Above the compensation temperature, there is a swapping of the dominant magnetic sublattice. That causes the change of the direction of the net magnetic moment. Also, there is an opposite alignment of magnetic sublattices in the external magnetic field due to the fact that net magnetic moment, which has the same direction as dominant sublattice, tends to be parallel with the external magnetic field.

2.2 Magnetic anisotropy

Magnetic anisotropy results from the dependence of the energy of a given magnetic moment on its orientation with respect to individual crystal axes. For uniaxial anisotropy, this energy can be expressed as [19]

$$E_a = K_a \sin^2 \theta \tag{2.1}$$

where K_a is the anisotropy constant (with respect to magnetic field H) for easy axis a and θ is the angle between the direction of magnetization and the direction of the easy axis a.

Anisotropy determines in which direction the magnetic moments spontaneously arrange; i.e. it indicates the direction of magnetization in the magnetic domains of ferro, ferri and antiferromagnets. It also affects the magnitude of the coercive force. The overall magnetic anisotropy of the system is affected by several factors. Anisotropy constant consists of three terms

$$K_a = K^a_{shape} + K^a_{elast} + K^a_{cryst}\,, \tag{2.2}$$

where K^a_{cryst} is magnetocrystalline anisotropy which is determined by the symmetry of the crystal, K^a_{shape} stands for shape anisotropy which is affected by the geometry of the sample and lastly, K^a_{elast} is magnetoelastic anisotropy. It is defined as

$$K^a_{elast} = \lambda_a \sigma_a\,, \tag{2.3}$$

where λ_a is the magnetostriction coefficient and σ_a is the strain applied parallel to the easy axis a. [20]

In the case of magnetically anisotropic materials, different direction of magnetization means different magnetic properties of the crystal. Two important directions in the crystal are distinguished. The axis along which the magnetization of the material is the easiest (minimum of the anisotropy energy) is called the *easy axis*. This direction is energetically favourable for spontaneous magnetization. When applying a magnetic field parallel to the easy axis, magnetic domains are oriented in the direction of the magnetic field. After switching off the magnetic field, magnetic domains stay ordered and the material has remanent magnetization (figure 2.3a). Second important axis, which is perpendicular to the easy axis, is called *hard axis*. When applying a magnetic field parallel to the hard axis (perpendicular to the easy axis), magnetic domains are again oriented in the direction of the magnetic field. However, after switching off the magnetic field, magnetic domains disorder into multiple directions. It is because the two opposite directions along an easy axis are usually equivalently easy to magnetize along. In this state the external magnetization of the material is almost equal to zero, i.e. there is almost no remanence (figure 2.3b).

Typical magnetization loops of ferrimagnetic material are shown in figure 2.3. In case of a magnetic field applied to a crystal parallel to the easy axis, there is non-zero magnetization in remanence and the coercivity field H_C. The magnetization in the hard axis is usually used to determine the anisotropy field (the point where magnetization reaches the values of M_S in this direction). At this point, the external magnetic field force all magnetic moments to lay in the direction parallel to the hard axis.

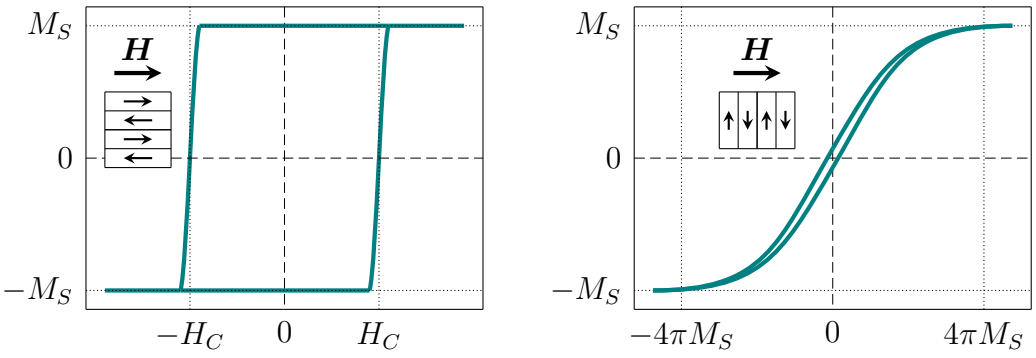

(a) easy axis (b) hard axis

Figure 2.3: Magnetization hysteresis loops with external magnetic field applied parallel to (a) easy axis (b) hard axis.

In the case of thin films, which is the case of this work, it is common to address the direction of magnetic anisotropy relatively to the surface of the sample. Hence the material with easy axis perpendicular to the surface of the sample is said to have perpendicular magnetic anisotropy (PMA).

3. Interaction between light and matter

3.1 Permittivity tensor

In general, optical response of matter can be macroscopically described by permittivity tensor $\boldsymbol{\varepsilon}$. Its knowledge allows to solve the wave equation and thus to obtain reflectivity coefficients, which are needed to calculate magneto-optical angles. Moreover, this process can be done backwards. This permits to calculate particular permittivity tensor elements of specific material from the knowledge of the magneto-optical Kerr angle.

It is a 3×3 tensor that has, generally, 9 independent (complex) elements

$$\boldsymbol{\varepsilon} = \begin{bmatrix} \varepsilon_{xx} & \varepsilon_{xy} & \varepsilon_{xz} \\ \varepsilon_{yx} & \varepsilon_{yy} & \varepsilon_{yz} \\ \varepsilon_{zx} & \varepsilon_{zy} & \varepsilon_{zz} \end{bmatrix}, \tag{3.1}$$

$$\varepsilon_{ij} = \varepsilon'_{ij} + i\varepsilon''_{ij}\,. \tag{3.2}$$

However, this general form can be significantly simplified by using specific symmetries.

When an external magnetic field is applied to the material, its permittivity tensor will be affected because of an induced anisotropy inside the sample. Perturbation of the permittivity tensor is usually small. Therefore elements of the permittivity tensor can be described within the Taylor series

$$\varepsilon_{ij} \approx \varepsilon_{ij}(0) + \left(\frac{\partial \varepsilon_{ij}}{\partial M_k}\right)_{M=0} M_k + \cdots\,, \tag{3.3}$$

where i, j, k each represent any index of the Cartesian basis x, y, z. The first term of equation (3.3) $\varepsilon_{ij}(0)$ represents the tensor elements when no external magnetic field is applied to the sample. The second term determines linear magneto-optical effects that are linear with respect to the magnetization $\boldsymbol{M} = (M_x, M_y, M_z)$. Because this thesis is working only with the linear magneto-optical Kerr effect, restriction to the first two terms is adequate.

Further important feature of the permittivity can be obtained from a time reversal symmetry (in the Cartesian system)

$$\varepsilon_{ij}(\boldsymbol{M}) = \varepsilon_{ji}(-\boldsymbol{M}) \tag{3.4}$$

MOKE is directly proportional to the vector of magnetization $\boldsymbol{M}$. For that reason, it is usually measured in 3 different geometries relative to the orientation of the magnetization vector $\boldsymbol{M}$ to the plane of incidence and sample surface: *polar*, which is in the main interest of this thesis, *longitudinal* and *transversal*. In the polar configuration, the magnetization vector of the sample is perpendicular to the sample surface. In longitudinal geometry, the magnetization vector lies in the plane of the sample and it is parallel with the plane of incidence. In the transversal configuration, the magnetization vector again lies in the sample surface

but it is perpendicular to the plane of incidence. In the first two cases, i.e. polar and longitudinal, the polarization of the light changes after the reflection. In the third case, only the intensity of incident p-polarized beam changes. [21] All three geometries can be seen in figure 3.1.

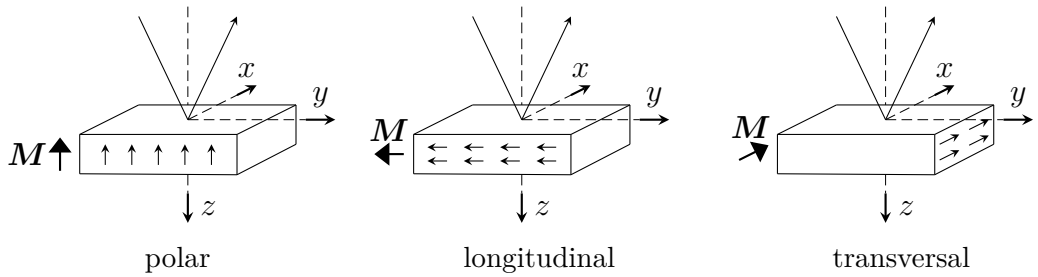

Figure 3.1: Three different configurations of magneto-optical Kerr effect (MOKE) with respect to the magnetization vector $\boldsymbol{M}$

After placing the sample into the magnetic field, optical anisotropy results in non-zero off-diagonal elements of the permittivity tensor (3.1). However, due to certain symmetries[1] (see [12]), permittivity tensor is simplified to the form

$$\boldsymbol{\varepsilon}_{polar} = \begin{bmatrix} \varepsilon_{xx} & \varepsilon_{xy} & 0 \\ -\varepsilon_{xy} & \varepsilon_{xx} & 0 \\ 0 & 0 & \varepsilon_{zz} \end{bmatrix} . \tag{3.5}$$

Because of the restriction to linear magneto-optical effects (see [22]), further simplification can be made ($\varepsilon_1 = \varepsilon_{xx} \approx \varepsilon_{zz}$; $i\varepsilon_2 = \varepsilon_{xy}$)

$$\boldsymbol{\varepsilon}_{polar} = \begin{bmatrix} \varepsilon_1 & i\varepsilon_2 & 0 \\ -i\varepsilon_2 & \varepsilon_1 & 0 \\ 0 & 0 & \varepsilon_1 \end{bmatrix} . \tag{3.6}$$

Equation (3.6) shows the permittivity tensor in case of polar geometry. It has only two independent complex elements ε_1 and ε_2.

Permittivity tensor for longitudinal (transversal) geometry can be obtained by rotating the coordinate system of polar configuration counterclockwise $\frac{\pi}{2}$ around x (y) axis

$$\boldsymbol{\varepsilon}_{longitudinal} = \begin{bmatrix} \varepsilon_1 & 0 & i\varepsilon_2 \\ 0 & \varepsilon_1 & 0 \\ -i\varepsilon_2 & 0 & \varepsilon_1 \end{bmatrix} , \tag{3.7}$$

$$\boldsymbol{\varepsilon}_{transversal} = \begin{bmatrix} \varepsilon_1 & 0 & 0 \\ 0 & \varepsilon_1 & i\varepsilon_2 \\ 0 & -i\varepsilon_2 & \varepsilon_1 \end{bmatrix} . \tag{3.8}$$

[23]: Relation between diagonal element of the permittivity tensor (3.6) and the normal refractive index n and the normal extinction coeficient k is

$$n^2 - k^2 = \varepsilon_1' , \tag{3.9a}$$

$$2nk = \varepsilon_1'' . \tag{3.9b}$$

[1] Voight symmetry theorem - it requires invariant coefficients of the tensor with respect to all transformations in the given group of symmetry. In this case, invariation of the permittivity tensor with respect to any rotation around the z axis.

Relation between off-diagonal element and refractive indices $n_\pm$ and the extinction coefficients $k_\pm$ of right (+ (RCP)) and left (– (LCP)) circularly polarized light is

$$(n_+ - n_-) + i(k_+ - k_-) = \frac{\varepsilon_2}{\sqrt{\varepsilon_1}}\,. \tag{3.10}$$

The Faraday rotation Ψ_F is half of the phase difference between the RCP and LCP waves and the Faraday ellipticity ϵ_F is the difference in absorption of the RCP and LCP waves:

$$\Psi_F = \frac{\pi}{\lambda}(n_+ - n_-) = \mathrm{Re}\left\{\frac{\pi\varepsilon_2}{\lambda\sqrt{\varepsilon_1}}\right\}, \tag{3.11}$$

$$\epsilon_F = \frac{\pi}{\lambda}(k_+ - k_-) = \mathrm{Im}\left\{\frac{\pi\varepsilon_2}{\lambda\sqrt{\varepsilon_1}}\right\}. \tag{3.12}$$

Reversely, ε_2' and ε_2'' can be written as

$$\varepsilon_2' = \frac{\lambda}{\pi}(n\Psi_F - k\epsilon_F) \tag{3.13a}$$

$$\varepsilon_2'' = \frac{\lambda}{\pi}(k\Psi_F + n\epsilon_F)\,. \tag{3.13b}$$

Consequently the Kerr rotation Ψ_K is equal to half of the phase difference between the RCP and LCP waves after reflection

$$\Psi_K = \tfrac{1}{2}(\Psi_+ - \Psi_-) = \mathrm{Im}\left\{\frac{\hat{r}_+ - \hat{r}_-}{\hat{r}_+ + \hat{r}_-}\right\},^{2} \tag{3.14}$$

where $\hat{r}_\pm = r_\pm e^{i\Psi_\pm}$ are the complex reflection coefficients. The Kerr ellipticity ϵ_K is equal to the ratio of minimum and maximum amplitude of the light reflected from the sample

$$\epsilon_K = -\frac{\hat{r}_+ - \hat{r}_-}{\hat{r}_+ + \hat{r}_-} = \mathrm{Re}\left\{-\frac{\hat{r}_+ - \hat{r}_-}{\hat{r}_+ + \hat{r}_-}\right\}. \tag{3.15}$$

Again, ε_2' and ε_2'' can be written as

$$\varepsilon_2' = -\Psi_K(3n^2k - k^3 - k) - \epsilon_K(n^3 - 3n^2k - n)\,, \tag{3.16a}$$

$$\varepsilon_2'' = \Psi_K(n^3 - 3nk^2 - n) - \epsilon_K(3n^2k - k^3 - k)\,. \tag{3.16b}$$

3.2 Optical transitions

Another important property of permittivity is its spectral dependence. It is originated from the interaction of light and matter through different microscopic mechanisms like electronic transitions, interactions of photons and excitons. A lot of phenomenological models are used for the approximative description of terms of the permittivity tensor. Below, two models that are used in this work are presented.

[2] for $\frac{\hat{r}_+ - \hat{r}_-}{\hat{r}_+ + \hat{r}_-} \ll 1$

3.2.1 Lorentz model

This classical model describes an interaction between light wave $\boldsymbol{E} = E_0 e^{i\omega t}$ and atom and it further enables to calculate the permittivity tensor. Atom in this model is described classically as a nucleus and one electron harmonically bonded to it.

When the light wave passes through the material, an electric field of the wave makes the electron deviate from its equilibrium position. That cause macroscopic polarization $\boldsymbol{P}$ in the material. It can be defined by the number of electrons N, the charge of the electron e and a displacement of the electron $\boldsymbol{r}$

$$\boldsymbol{P} = Ne\boldsymbol{r}\,. \tag{3.17}$$

Polarization can be also defined via relative permittivity ε_r, permittivity of vacuum ε_0 and external electric field $\boldsymbol{E}$ as

$$\boldsymbol{P} = \varepsilon_0(\varepsilon_r - 1)\boldsymbol{E}_0 = \varepsilon_0\boldsymbol{\chi}\boldsymbol{E}\,, \tag{3.18}$$

where $\boldsymbol{\chi} = \varepsilon_r - 1$ is the tensor of susceptibility.

The equation of motion of the system nucleus – electron, which is excited by the light wave propagating along the z axis is as follows

$$\frac{\mathrm{d}^2\boldsymbol{P}}{\mathrm{d}t^2} + \Gamma\frac{\mathrm{d}\boldsymbol{P}}{\mathrm{d}t} + {\omega_0}^2\boldsymbol{P} = \varepsilon_0{\omega_p}^2\boldsymbol{P}\,, \tag{3.19}$$

where Γ is a damping constant, ${\omega_p}^2 = \frac{Ne^2}{m\varepsilon_0}$ is the plasma frequency and ${\omega_0}^2 = \frac{\kappa}{m_e}$, where κ is the toughness of the bond (*spring*) between the nucleus and electron and m_e is the effective mass of the electron.

Equation (3.19) is the differential equation for harmonic oscillator. Because of this, its solution can be found in the form of

$$\boldsymbol{P}(\omega, t) = \boldsymbol{P}(\omega)e^{i\omega t}\,. \tag{3.20}$$

After solving the equation above, the polarization is then

$$\boldsymbol{P}(\omega) = \frac{\varepsilon_0{\omega_p}^2}{{\omega_0}^2 - \omega^2 + i\omega\Gamma}\boldsymbol{E}_0\,. \tag{3.21}$$

With help of equation (3.18), the description of the diagonal term of the permittivity tensor is as follows

$$\varepsilon_1 = 1 + \frac{{\omega_p}^2}{{\omega_0}^2 - \omega^2 + i\omega\Gamma}\,. \tag{3.22}$$

This relation describes the permittivity for N electrons with the same binding force. In materials, there are plenty of electrons with different binding forces, and electrons with different binding forces behave slightly different. Therefore, the optical response of the whole material can be written as

$$\varepsilon_1 = 1 + \sum_j \frac{a_j{\omega_{pj}}^2}{{\omega_{0j}}^2 - \omega^2 + i\omega\Gamma_j}\,, \tag{3.23}$$

where a_j are different oscillator strengths, which are the probabilities of absorption/emission of electromagnetic radiation in transitions between energy levels of atoms of same binding force.

Although this model uses a basic model of an atom, optical dispersion is usually very well described. It has some limits as it, for example, significantly loose accuracy near an absorption edge of a material. For that reason several models were invented with slight correction from the original Lorentz model (Tauc-Lorentz, Cody-Lorentz). Here Tauc-Lorentz model is presented.

3.2.2 Tauc-Lorentz model

To improve the Lorentz model near the absorption edge, Tauc-Lorentz model add another parameter ω_g, frequency of the band gap. There is different behaviour of imaginary part of ε_1 below and above this frequency as it can be seen in equations (3.25).

$$\mathrm{Im}\{\varepsilon_1\}(\omega) = \begin{cases} \dfrac{(\omega-\omega_g)^2}{\omega^2}, & \text{for } \omega > \omega_g \quad (3.24) \\ 0, & \text{for } \omega < \omega_g \quad (3.25) \end{cases}$$

Real part of ε_1 is then calculated with use of Kramers-Kronig relations.

3.3 Magneto-optical transitions

Microscopic theory of the permittivity tensor relates elements ε_1 and ε_2 to energy-level splittings of degenerated states of non-zero angular momentum and transition probabilities of electrons. Because of spin-orbital interaction (coupling) and exchange field effect, the Zeeman effect makes one (or more) electron level split into two.[3] Consider two types of optical transitions: splitting of the excited, *diamagnetic*, state, so-called *double transitions* and splitting of the ground, *paramagnetic*, state, so-called *single transitions*.[24] Each level has a slightly different energy and is solely for one type of polarization due to the selection rules.

Double transitions (diamagnetic) Spin-allowed charge transfer transitions, that are often very intense and are usually found in the UV region with reach to the visible with a tail, are often this type of transition. Spectral dependence of the off-diagonal element of the permittivity tensor ε_2 is described as [23]

$$\varepsilon_2(\omega) = \varepsilon_2'(\omega) - i\varepsilon_2''(\omega) = \frac{\omega_p^2 f \Delta L}{2\omega_0} \frac{(\omega_0-\omega)^2 - \Gamma_0^2 + 2i\Gamma_0(\omega_0-\omega)^2}{\left[(\omega_0-\omega)^2+\Gamma_0^2\right]^2}, \qquad (3.26)$$

where ω_p is the plasma frequency defined as $\omega_p^2 = \frac{4\pi N e^2}{m}$, where e and m are charge and mass of the electron and N is the number of octahedral ions per cm^3. Δ is the separation between the levels which is caused by spin-orbit coupling, $L = [\frac{n^2+2}{3}]^2$ is the Lorentz-Lorentz local field correction, f is the oscillator strength defined as $f = \frac{2m\omega_0}{Le^2}|p_e^x|^2$, where $|p_e^x|^2$ is the electric dipole matrix element between

[3] It breaks the degeneracy in the energies. It does not create more states.

ground and excited state and ω_0 and Γ_0 are the center frequency and half-width at half-height of the transition, consequently. It is assumed that $\Delta \ll \Gamma_0$.

The real part $\varepsilon_2'(\omega)$ has its maximum at $\omega = \omega_0$

$$(\varepsilon_2')_{max} = -\frac{\omega_p^2 f \Delta L}{2\omega_0 \Gamma_0^2} \tag{3.27}$$

and the imaginary part $\varepsilon_2''(\omega)$ behaves dispersive around ω_0 and equals zero at ω_0

$$\varepsilon_2''(\omega_0) = 0\,. \tag{3.28}$$

Single transitions (paramagnetic) Examples of this type of transition are spin- and electric-dipole-forbidden crystal field transitions.[23] For these transitions, ε_2 behaves as [23]

$$\varepsilon_2(\omega) = \varepsilon_2'(\omega) - i\varepsilon_2''(\omega) = \frac{\omega_p^2 f df L}{2} \frac{\omega(\omega_0^2 - \omega^2 - \Gamma_0^2) + i\Gamma_0(\omega_0^2 + \omega^2 + \Gamma_0^2)}{\omega_0\left[(\omega_0^2 + \omega^2 + \Gamma_0^2)^2 + (2\omega\Gamma_0)^2\right]}\,, \tag{3.29}$$

where $df = \frac{f_- - f_+}{f_- + f_+} = \frac{f_- - f_+}{2f}$ is the fractional dichroism, where f^+, f^- are oscillator strengths for RCP and LCP light, respectively.

In this case, the real part $\varepsilon_2'(\omega)$ behaves dispersive around ω_0 and is zero at $\omega = \omega_0$

$$\varepsilon_2'(\omega_0) = 0\,. \tag{3.30}$$

The maximum of the imaginary part is also at $\omega = \omega_0$ [23]

$$(\varepsilon_2'')_{max} = \frac{\omega_p^2 f df L}{\omega_0} = df\,(\varepsilon_1'')_{max}\,. \tag{3.31}$$

The formula (3.29) is strongly dependent on temperature because of the effect of Boltzmann population at split levels. Therefore,

$$\Gamma_0 \approx \frac{1}{k_B T}\,. \tag{3.32}$$

Diagram of this dependence is shown in figure 3.3.

Spectral shapes of the above-mentioned transition are illustrated in figure 3.2. It provides a useful tool for the interpretation of experimental spectra.

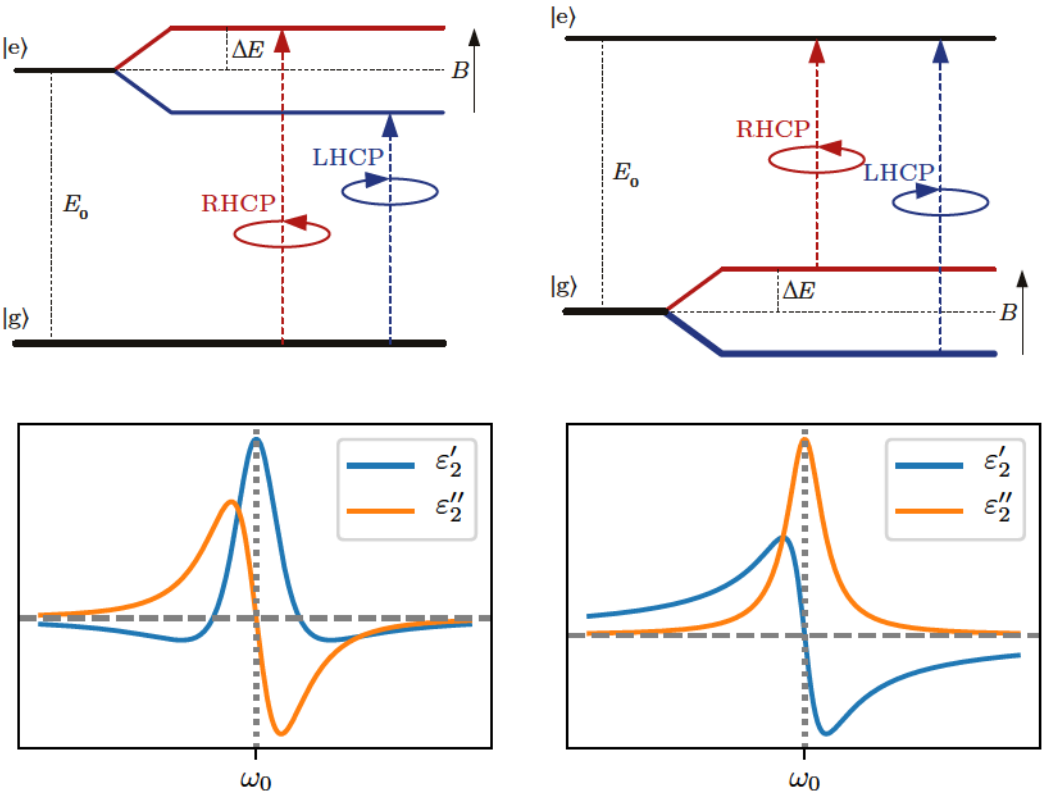

(a) Double (diamagnetic) (b) Single (paramagnetic)

Figure 3.2: Schemes of magneto-optical transition and calculated spectra of ε_2', ε_2'' for (a) double (diamagnetic) and (b) single (paramagnetic) transition.[20]

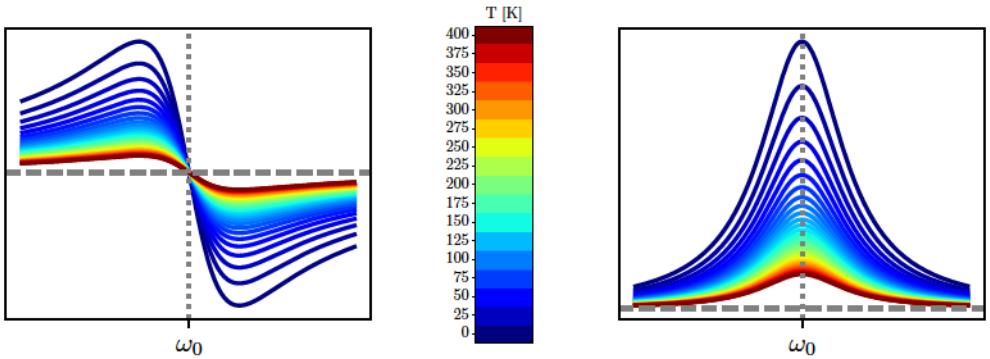

(a) ε_2' (b) scale (c) ε_2''

Figure 3.3: Temperature dependence of (a) real and (c) imaginary part of off-diagonal element of permittivity tensor.[20]

Part II

Experimental methods

This part provides a short overview of the experimental methods and techniques used in this work and a brief introduction to studied materials. Subsequently, there is a general description of ferrimagnetic garnets and the metal-organic decomposition (MOD) deposition technique, which was used for the preparation of samples in this work.

4. Optical and magneto-optical characterization

4.1 Magneto-optical effects measurements

Magneto-optical spectroscopy is an experimental technique where the dependence of a magneto-optical effect on the energy of incident light is investigated. In this case, the sample is in the magnetic field that completely saturates the sample, i.e. the direction of the magnetization vector has the same direction as the direction of the external magnetic field. It may then be assumed that the magnetization vector has only the polar or longitudinal component depending on the direction of the external magnetic field. In the state of complete saturation, the given effect is maximal and therefore the easiest to measure.

MO spectroscopy therefore allows to measure the spectral dependence of magneto-optical angles Ψ_K (Ψ_F) and ϵ_K (ϵ_F) which can be used to determine the off-diagonal elements of the permittivity tensor.

There are a number of both direct and indirect experimental methods for determining the Kerr/Faraday angle. These are divided into *intensive* and *modulating* methods.

In this work, the intensive **rotating analyzer technique** is used to measure the magneto-optical Kerr effect. The magnitude of the MOKE is obtained from the dependence of the intensity of light in the detector upon the mutual rotation of polarizers, between which the sample is placed in a magnetic field. A schematic of this experimental setup is shown in figure 4.1. For each wavelength and a given angle of incidence of light on the sample, two parameters (Ψ_K and ϵ_K) are obtained, which describe the change in the polarization state at the reflection from the sample as a complex ratio of the reflectivity of the p- (parallel) and s- (perpendicular) components of polarization (see 1.54).

Jones formalism, introduced in section 1.3, will be used for the description of this setup. First, the wide-spectrum light is emitted from the lamp. It then passes through a polarizer P, reflects off a sample S, which is in the magnetic field

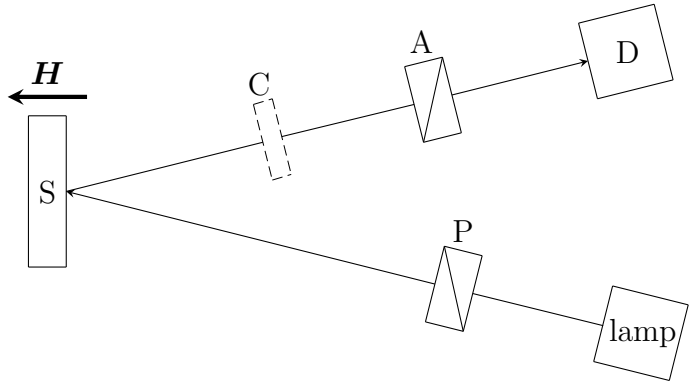

Figure 4.1: Schematic of the Kerr effect measurement set-up. Light wave passes through the polarizer P, reflects off the sample S, which is in magnetic field H, and then continues to the phase plate C, the analyzer A and into the detector D.

H, and it passes through an optional quarter phase plate C, analyzer A and goes into a detector D.

The light wave after the passage through the whole setup can be described by the Jones vector $\boldsymbol{J}^{(O)}$. It is determined by multiplying the Jones vector of the incident wave $\boldsymbol{J}^{(I)}$ (1.28) with the linear polarizer matrices (1.47), phase plate matrix (1.49) and the reflection matrix of the sample (1.41). The general expression is as follows:

$$\boldsymbol{J}^{(O)} = \begin{bmatrix} \cos^2\varphi & \sin\varphi\cos\varphi \\ \sin\varphi\cos\varphi & \sin^2\varphi \end{bmatrix} \begin{bmatrix} e^{i\Gamma/2} & 0 \\ 0 & e^{-i\Gamma/2} \end{bmatrix} \begin{bmatrix} r_{ss} & r_{sp} \\ r_{ps} & r_{pp} \end{bmatrix} \begin{bmatrix} \cos^2\varphi & \sin\varphi\cos\varphi \\ \sin\varphi\cos\varphi & \sin^2\varphi \end{bmatrix} \boldsymbol{J}^{(I)}. \quad (4.1)$$

For the specific setup used in this work, the above-mentioned matrices will change. The polarizer P is set to 90° angle. Therefore the light behind the polarizer is p- polarized. The resulting Jones vector is then

$$\boldsymbol{J}^{(O)} = \begin{bmatrix} \cos^2\varphi & \sin\varphi\cos\varphi \\ \sin\varphi\cos\varphi & \sin^2\varphi \end{bmatrix} \begin{bmatrix} e^{i\Gamma/2} & 0 \\ 0 & e^{-i\Gamma/2} \end{bmatrix} \begin{bmatrix} r_{ss} & r_{sp} \\ r_{ps} & r_{pp} \end{bmatrix} \begin{bmatrix} 0 \\ 1 \end{bmatrix}. \quad (4.2)$$

The intensity I measured by the detector can be written as [12]

$$I \approx \left|(\boldsymbol{J}^{(O)})^* \boldsymbol{J}^{(O)}\right| = \frac{R}{2}[\sin^2\varphi + |\Phi_K|^2 \cos^2\varphi + \sin(2\varphi)\,\mathrm{Re}\{\Phi_K e^{i\Gamma}\}], \quad (4.3)$$

where $R = |r_{pp}|^2$ is the reflectivity of the sample, φ is the angle of rotation of the polarizer and Γ is the retardance of the phase plate. For small values of the MOKE, second-order term $|\Phi_K|^2$ can be approximated with $\Psi_K - i\epsilon_K$. For measured intensity then applies [12]

$$I \approx \frac{R}{2}[\sin^2\varphi + (\Psi_K \cos\Gamma + \epsilon_K \sin\Gamma)\sin(2\varphi)]. \quad (4.4)$$

In case of not using the phase plate, Γ is equal to 0; the intensity then depends only on Kerr rotation Ψ_K, the reflectivity of the sample and on the angle of rotation of the polarizer. The Kerr rotation Ψ_K is then fitted for every pixel of the CCD detector and for the measured angle dependence.

Another intensive method is the so-called **differential method**. This method was used for measuring Faraday effect hysteresis loops. Schematic of this set-up is in figure 4.2. In this method, the Faraday rotation is measured using the difference between the intensities of the beams that go through a Wollaston prism. Generally, the Faraday effect occurs in samples that are in the magnetic field. Magnetic field induces birefringence that results in a rotation of the polarization plane of linearly polarized light. Empirically, it applies

$$\phi = VBd, \quad (4.5)$$

where ϕ is the angle of rotation, d is the length of the sample, B is the magnetic field, which is parallel to the direction of propagation of light wave and V is the Verdet constant. Verdet constant is dependent on the temperature, the wavelength of the light and the refractive index of the material.

In this set-up, polarized light is passing through the sample, the half wave plate, the Wollaston prism and into two photodiodes. Optional quarter wave plate can be added for measuring Faraday ellipticity instead of Faraday rotation. Half wave plate is here used as polarization rotator. It helps to cancel the constant polarization effects that might occur in the optical setup. [25] The Wollaston prism here serves as a polarizing beam splitter, which separates the incident beam into two *s*- and *p*- polarized beam The Jones vector $\boldsymbol{J}^{(O)}$ of the light wave after the passage of the whole setup can be again determined by multiplying the Jones vector of the incident wave $\boldsymbol{J}^{(I)}$ (1.28) with the linear polarizer matrix (1.47), transmission matrix of the sample (1.44), the phase plate matrix (1.49) and the Wollaston prism matrix (rotated at an angle α)

$$\boldsymbol{J}^{(O)} = \begin{bmatrix} \cos\alpha & -\sin\alpha \\ \sin\alpha & \cos\alpha \end{bmatrix} \begin{bmatrix} e^{i\Gamma/2} & 0 \\ 0 & e^{-i\Gamma/2} \end{bmatrix} \begin{bmatrix} t_{ss} & t_{sp} \\ t_{ps} & t_{pp} \end{bmatrix} \begin{bmatrix} 1 \\ 0 \end{bmatrix} . \tag{4.6}$$

The Wollaston prism is rotated at angle $\alpha = 45°$ because in this setting, when no magnetic field is applied (i.e. isotropic sample), measured intensities for *s*- and *p*-polarized waves are the same. The following process is similar to one mentioned above. The crucial part of this method is when the measured intensities on the photodiodes are subtracted and then divided by their sum. After some algebraic operations (can be found in [25]), the following formula is obtained

$$-\frac{I_{diff}}{2I_{sum}} = \Psi_{Fs} - 2\kappa\,, \tag{4.7}$$

where κ is the angle of rotation of the half wave plate and Ψ_F is the Faraday angle.

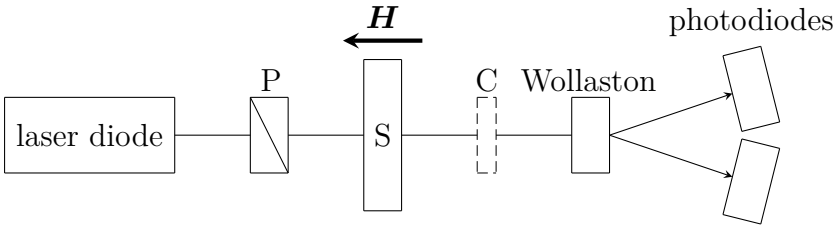

Figure 4.2: Schematic of magnetic Faraday loops measurement set-up. Light wave passes through the polarizer P, sample S, which is in the magnetic field H. The light wave then continues to the half-wave plate C, through the Wollaston prism and into the two photodiodes.

Modulating methods are based on the use of various optical elements that regularly, harmonically in time, change the polarization state of transmitted light. The measured intensity then contains members which oscillate over time and which are separated from the detected signal by a lock-in amplifier and synchronous detection. The advantage of these methods is that the resulting signal-to-noise ratio is higher. For example, the angle of rotation of a polarizing ellipse (azimuth) can be modulated using a Faraday cell or the ellipticity can be modulated using a photoelastic modulator.

4.2 Spectroscopic ellipsometry

Spectroscopic ellipsometry is mainly used in the analysis of the optical response of both thin films and bulk materials. As in magneto-optical spectroscopy, the change in polarization of light is measured when reflected from a sample that is no longer in a magnetic field. This method measures this change in polarization state for a given wavelength. Spectroscopic ellipsometry can determine not only the optical constants of individual layers, such as refractive index and absorption coefficient, but also their thicknesses and other structural properties. An ellipsometer, which is an instrument for measuring the above-mentioned quantities, usually consists of a light source, a polarizer, one or two compensators, an analyzer and a detector.

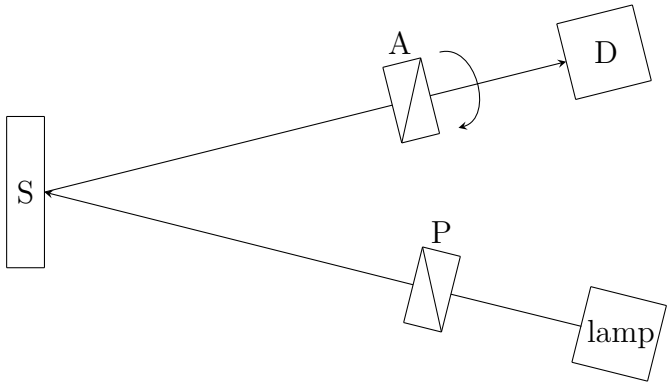

Figure 4.3: Schematic of ellipsometry set-up. Light wave passes through the polarizer P, reflects off the sample S; it then continues to the rotating analyzer A and into the detector D.

The simplest arrangement of these components (without compensators) is an ellipsometer with a rotating analyzer. A scheme of this set-up can be seen in figure 4.3. In this type of ellipsometer, the light wave passes through a polarizer, which forms an angle ψ with the s- polarization axis. Furthermore, the light is reflected from the sample and passes through an analyzer, which is at angle ζ relative to the s- polarization axis, and then enters a detector measuring its intensity. The angle of rotation of the polarizer ψ must be such that the s- and p- polarized component of the wave can pass through. The light wave, after passing through the whole set-up, can be described by the Jones vector $\boldsymbol{J}^{(O)}$, which is determined by multiplying the polarizer matrix (1.47), the reflection matrix (1.41) and the Jones vector of the incident light (1.28):

$$\boldsymbol{J}^{(O)} = \begin{bmatrix} \cos^2\zeta & \sin\zeta\cos\zeta \\ \sin\zeta\cos\zeta & \sin^2\zeta \end{bmatrix} \begin{bmatrix} r_{ss} & r_{sp} \\ r_{ps} & r_{pp} \end{bmatrix} \begin{bmatrix} \cos\psi \\ \sin\psi \end{bmatrix}, \tag{4.8}$$

Because the sample is no longer in magnetic field and therefore it is isotropic[1], reflexion matrix (1.41) is diagonal. The intensity arriving to the detector is [26]

$$I \approx \left|\boldsymbol{J}^{(O)}\right|^2 = |r_{pp}|^2 \cos^2\psi\cos^2\zeta + |r_{ss}|^2 \sin^2\psi\sin^2\zeta - \frac{1}{4}(r_{pp}r_{ss}^* + r_{ss}r_{pp}^*)\sin 2\psi \sin 2\zeta \tag{4.9}$$

[1]Samples measured in this thesis are isotropic when no magnetic field is applied. However, there are also plenty of materials that are anisotropic even in zero magnetic field.

From each intensity measurement for each wavelength range and the angles selected at the beginning of the experiment, two parameters are obtained (Ψ – the angle of rotation of the ellipse and Δ – ellipticity [i.e. flattening of the ellipse]). These parameters describe the change in polarization state when reflected from a sample as a complex ratio of the reflectivity of the *p*- (parallel) and *s*- (perpendicular) components of polarization. These two parameters are usually expressed in terms of the ratio of the amplitude reflection coefficients as

$$\rho = -\frac{r_{pp}}{r_{ss}} =: \tan\Psi e^{i\Delta}\,, \tag{4.10}$$

where ρ denotes the overall change in the polarization state of a given light wave. In this case, the intensity may be shown to be proportional to [26]

$$I \approx 1 - \eta\sin 2\zeta + \xi\cos 2\zeta\,, \tag{4.11}$$

where

$$\eta = 2\frac{\tan\Psi\cos\Delta\tan\psi}{\tan^2\Psi + \tan^2\psi}\,, \tag{4.12a}$$

$$\xi = \frac{\tan^2\Psi - \tan^2\psi}{\tan^2\Psi + \tan^2\psi}\,. \tag{4.12b}$$

From the measurement of intensity, coefficients η and ξ can be extracted. Afterwards, equations (4.12) can be inverted as

$$\tan\Psi = \sqrt{\frac{1+\xi}{1-\xi}}|\tan\psi|\,, \tag{4.13a}$$

$$\cos\Delta = \frac{\eta}{\sqrt{1-\xi^2}}\operatorname{sign}\psi\,. \tag{4.13b}$$

For a simple bulk, r_{ss} and r_{pp} in (4.10) can be substitued with expressions from Fresnel equations

$$r_{ss} = \frac{n_1\cos\psi_i - n_2\cos\psi_r}{n_1\cos\psi_i + n_2\cos\psi_r} \tag{4.14a}$$

$$r_{pp} = \frac{n_2\cos\psi_i - n_1\cos\psi_r}{n_2\cos\psi_i + n_1\cos\psi_r}\,, \tag{4.14b}$$

where $n_1 = \sqrt{\varepsilon_1}$ is the refractive index of the environment in which the sample is situated and $n_2 = \sqrt{\varepsilon_2}$ is the refractive index of the sample. $\varepsilon_{1,2} = \varepsilon_{\mathrm{Re}} + i\varepsilon_{\mathrm{Im}}$ is real and imaginary part of permittivity and $\sqrt{\varepsilon_{1,2}} = N = n + ik$, where n is real part of the refractive index and k is an exctinction coefficient.

The ellipsometer[2] used for the measurement of the ellipsometric data in this thesis uses in fact two compensators, which allows measurements of the full Mueller matrices. As this is not the interest of this thesis, a simpler, yet sufficient, set-up has been presented.

Refractive index calculation shown above was made just for single interface between ambient and material (semi-infinite bulk). However, this thesis works with

[2]RC2 Woollam

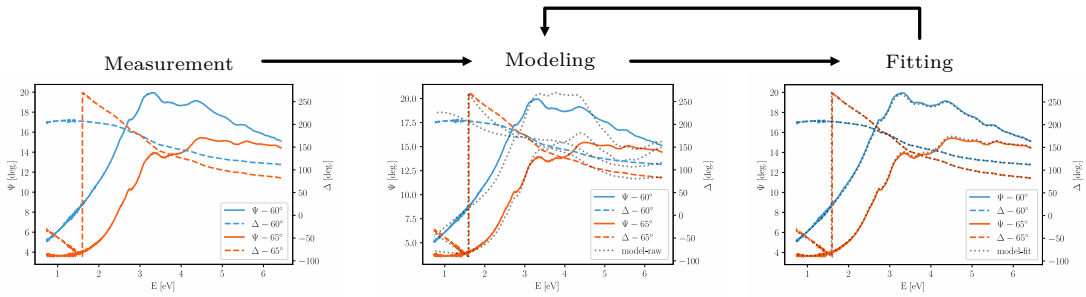

Figure 4.4: Schematic of ellipsometry data processing. The figure on the left shows experimental data. The second figure shows experimental data with the chosen model. The figure on the right shows the fitted model onto the experimental data. [20]

samples that are made as a thin layers deposited on substrates. Hence, multiple reflections within the sample need to be considered. Therefore, the complex index of refraction has to be numerically modelled with computer software. Modelling of measured ellipsometric angles Ψ and Δ is done within few steps. Measured data are compared with prediction calculated from the model of the studied structure. This model contains optical properties and thicknesses for each layer of the sample. The starting model is made out of knowledge from other scientific methods[3] and it is being improved throughout the whole process by varying its parameters. This process is being repeated until a satisfactory match is reached (see figure 4.4). The final model contains the thickness of the sample, its optical properties, roughness, inhomogeneities, etc. [20]

[3] more information can be found in [27, 28]

5. Ferrimagnetic garnets and their preparation

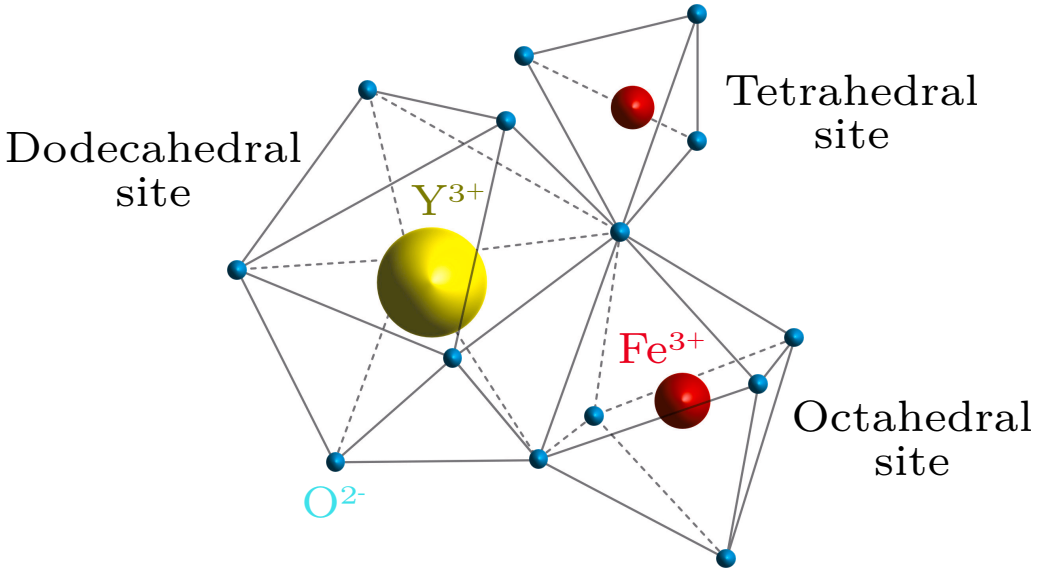

Figure 5.1: Schematic of crystallographic structure of yttrium-iron garnet ($Y_3Fe_5O_{12}$). Sublattices, which are filled with iron ions are octahedral and tetrahedral and yttrium filled site is dodecahedral. [20]

5.1 Garnet structure

Garnets are a very large group of materials that have many naturally occurring representatives (e.g. Pyrope– $Mg_3Al_2[SiO_4]_3$). This group enables the synthesis of completely new materials with new, as yet unprecedented, physical properties. They are dielectric oxides with very high hardness, excellent optical properties, especially in the visible and infrared regions of the electromagnetic spectrum, and very high chemical and structural stability. This work focuses on ferrimagnetic garnets (iron-based magnetic garnets). The general formula is $A_3B_2C_3O_{12}$.[1] The basic crystallographic structure of garnets is formed by a cubic elementary cell in which there are 3 sublattices of oxygen atoms: *dodecahedral* (A_3, occupied by three yttrium ions[2]), *octahedral* (B_2, occupied by two iron ions[2]) and *tetrahedral* (C_3, occupied by three iron ions[2]). Example of material that forms such structure is yttrium-iron garnet ($Y_3Fe_5O_{12}$) whose crystallographic structure is shown in figure 5.1. Both metal ions (Y^{3+} and Fe^{3+}), which are present in the structure, are trivalent, which makes YIG exceptionally suitable materials for their investigation

[1] A stands for any chemical element from the 3b group of the periodic table of elements or a rare earth element (*f* elements (lanthanoids)).

[2] for the case of yttrium-iron garnet ($Y_3Fe_5O_{12}$)

by magnetic and magneto-optical methods. The optical and magneto-optical response of these materials is then defined by the electron transitions of iron ions in different sublattices due to the different crystal field. [23]

In addition, different ions in 3 sublattices can be substituted by different elements and therefore change the magnetic, optical and magneto-optical properties of the garnet. Ions that most likely occupy octahedral sites (B_2) are Al^{3+}, Ga^{3+} or larger In^{3+} ion. The second group of substituents are elements from 3b group of the periodic table of elements or rare earth elements, also known as lanthanoids or *f* elements. Their ions substitute ions at dodecahedral site (A_3).[3] The presence of *f* shell electrons results in coupling with *d* electrons, which changes the ferrimagnetic character of the garnet. The most significant feature is the appearance of the compensation temperature, which is not present in garnets without magnetic element in the dodecahedral site. In the field of magneto-optics, the most important substituent for Y^{3+} is Bi^{3+}. This atom achieves an enormous increase of magneto-optical response via large spin orbit coupling. However, due to its size, it is very complicated to fully substitute Y^{3+} ion, yet it can be done. [29]

Physical properties of ferrimagnetic garnets can also be altered by partial replacement of iron atoms. It turns out that with different iron ratios in the individual sublattices, the compensation temperature of these materials changes. [11]

5.2 Metal-organic decompositon

Metal-organic decomposition (MOD) is a method of sample preparation, during which a metal-organic solution of the desired material is applied to a predetermined substrate (glass, gadolinium gallium garnet ($Gd_3Ga_5O_{12}$) (GGG)).

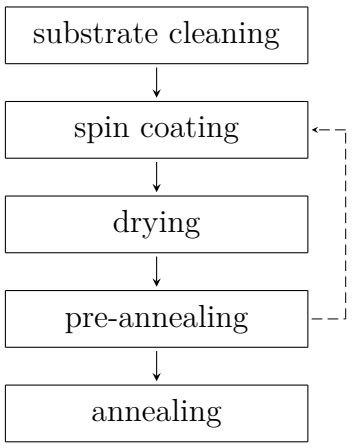

Figure 5.2: Diagram of metal-organic decomposition.

The starting materials are metal-organic compounds of desired elements that are dissolved in a suitable solvent. Solutions are then mixed in a ratio that depends on the desired final stoichiometry of the final sample. This solution is applied to a heated substrate that spins. Due to the centrifugal force, the

[3]Location of substitution is very sensitive to conditions of deposition. Therefore, it can be varied by deposition parameters.

solution homogeneously spreads over the entire substrate and it depends on the concentration of the solution, the speed and the time of rotation, how thick the layer of the material remains on the substrate. The sample is then transferred to a one or two "hot-plates", where the solvent is evaporated and then the metal-organic compounds gradually decompose and make final layer (*pre-annealing*). After this step, only pure material (here pure garnet) remains on the substrate, but it is still not a crystal. This is accomplished by enclosing the sample in the electric furnace, where the amorphous material becomes a crystal (*annealing*). The diagram of the method is shown in figure 5.2.

The quality of the sample is dependent on many factors: starting solution (stoichiometry), proper solvent (crystallinity, grain size), substrate temperature (speed of crystallization), speed of rotation (thickness of the film, homogeneity), atmosphere in the electric furnace (crystallinity), etc.

More details about MOD can be found in [30, 31].

Part III

Experimental results

This thesis focuses on the study of two groups of ferrimagnetic garnets. The first group of samples consists of yttrium-iron gallium garnet ($Y_3Fe_4Ga_1O_{12}$) in which the effect of different annealing temperatures and different orientation of the substrate on the optical and magneto-optical properties was examined. Bismuth doped neodymium-iron gallium garnets with different ratio of Nd and Bi ($Nd_xBi_{3-x}Fe_4Ga_1O_{12}$) are in the second group of samples. These samples were studied on how annealing temperature and the ratio of Nd and Bi change their optical, MO and magnetic properties.

6. $Y_3Fe_4Ga_1O_{12}$ on $Gd_3Ga_5O_{12}$

6.1 Preparation

The starting point of this study was to prepare four different thin samples of $Y_3Fe_4Ga_1O_{12}$ that would vary in substrates and annealing temperatures using metal-organic decomposition (MOD) method (see section 5.2). All four thin films were grown on gadolinium gallium garnet ($Gd_3Ga_5O_{12}$) with orientations (100) and (111). The concentration of solutions used for the deposition was 3 %. The rotation velocity of the spin coating was 3000 rpm[1] and the duration of this process was 30 seconds. Afterwards, the substrate with the solution was dried on the hot plate for 10 minutes at 100 °C. The final layer was made by decomposition, which was done at temperature 430 °C for 10 minutes. Good crystallinity was achieved by annealing the sample in the electric furnace for 3 hours at 750/800 °C. Parameters of prepared samples are listed in the table 6.1.

Table 6.1: $Y_3Fe_4Ga_1O_{12}$

material	substrate orientation	annealing temperature	layer thickness[2]	roughness[2]
$Y_3Fe_4Ga_1O_{12}$	100	750 °C	9.67 nm	2.44 nm
	100	800 °C	10.44 nm	1.24 nm
	111	750 °C	7.96 nm	0.04 nm
	111	800 °C	10.46 nm	1.46 nm

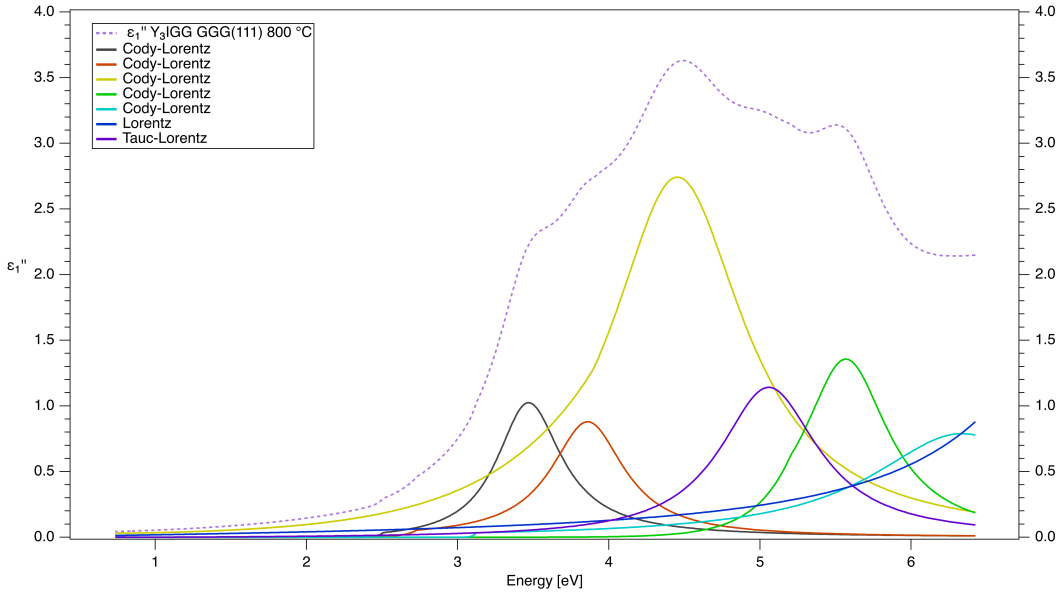

Figure 6.1: Oscillators used for the characterization of sample $Y_3Fe_4Ga_1O_{12}$ on GGG(111) substrate (annealing temperature 800 °C).

[1] rotation per minute
[2] values from ellipsometry measurements

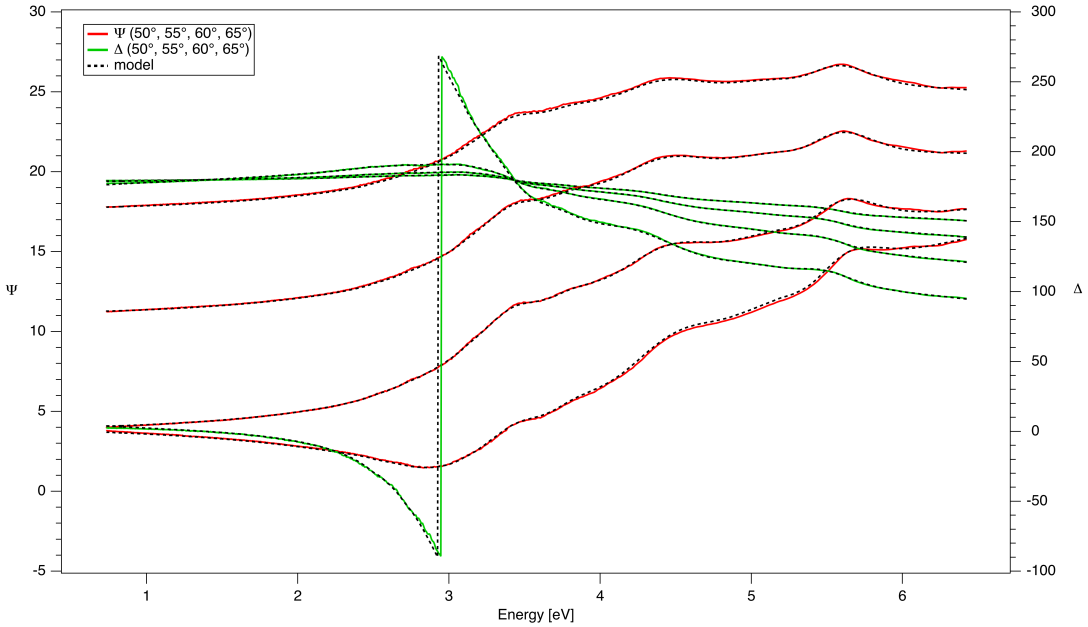

Figure 6.2: Fit of the optical constants Ψ and Δ of the sample $Y_3Fe_4Ga_1O_{12}$ on GGG(111) substrate (annealing temperature 800 °C).

6.2 Optical properties

Optical constants together with thickness and roughness of the samples were obtained using spectroscopic ellipsometry in a range of incident angles between 50° and 65° with a step of 5°. Because the samples were translucent, the backside of the substrate had to be roughened using a diamond pen and a grinder to avoid backside reflections. Optical constants of the GGG were obtained in different measurement on bare substrate. Measured data were firstly fitted with a mathematical B-spline model [32, 33] and then parameterized using a combination of 7 Lorentz, Cody-Lorentz and Tauc-Lorentz oscillators. The oscillators for one sample are shown in figure 6.1. Oscillators for other samples are similar. The result of the fit is shown in figure 6.2. The fit is in good agreement with reported results from [34]. The most visible difference between the results from [34] and in figure 6.1 is the height of the main oscillator at 4.4 eV in comparison with the others. This might be due to the presence of Ga. It can substitute some of the Fe^{3+} ions at, preferably [35, 36], tetrahedral site and therefore weaken the iron-iron superexchange interaction. The final optical constants are shown in figure 6.3.

In general, the shape of optical constants in the spectrum is similar to that which was measure elsewhere [23, 37]. According to [38] and later [34], the weakest absorption band at the energy 2.7 eV are caused by the bi-exciton transitions; simultaneous crystal field transitions of 2 neighbouring ions. A series of transitions in spectrum from 3 to 3.4 eV and the peak at 5.5 eV are associated with iron-to-iron sublattice charge transfer bands where it is expected that the electron transfers from tetrahedral Fe^{3+} site to octahedral Fe^{3+} site.[34] In this transition between two iron ion, the oxygen ion O^{2-} is the mediator of the superexchange interaction.[34] In the range of energy 3.4 to 4.3 eV several absorption bands are visible. They originate from the mixture of Fe^{3+}–Fe^{3+} charge transfer transitions

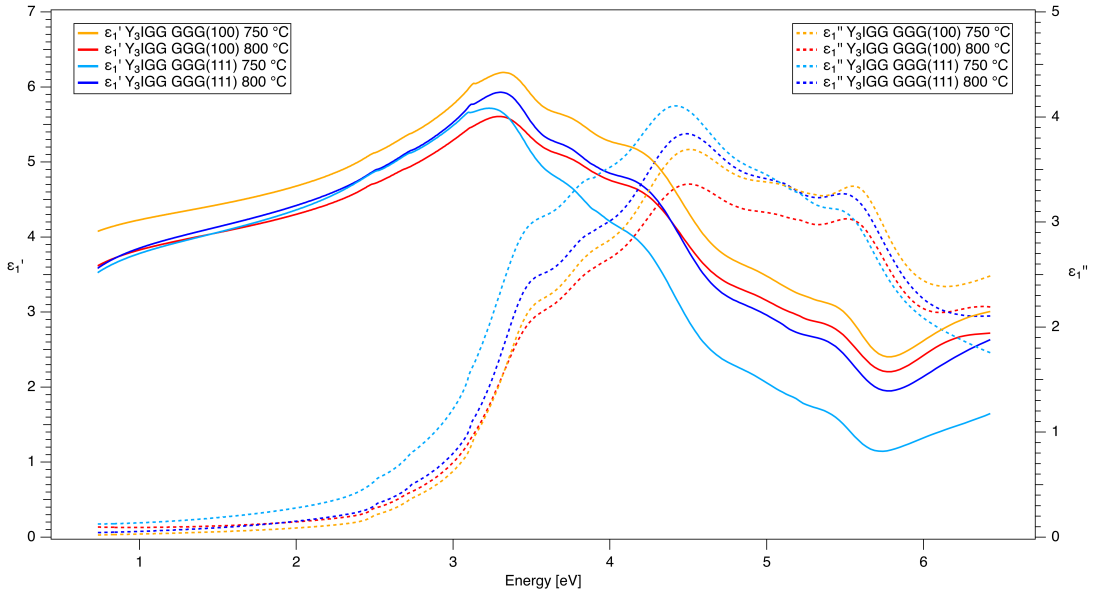

Figure 6.3: Spectral dependencies of the diagonal elements of the permittivity tensors of $Y_3Fe_4Ga_1O_{12}$ on GGG substrates with different orientations.

forming Fe^{4+}–Fe^{2+} pair, and O^{2-}–Fe^{3+} charge transfer transitions.[34] The biggest peak around 4.4 eV arises from the O^{2-}(2p)–Fe^{3+}(3d) transition. The strongest, semiconductor-like, optical transitions occur around 8 eV. These transitions most likely involve transitions between oxygen O^{2-}(2p) band and iron Fe^{3+}(4s) band.[39]

6.3 Magneto-optical properties

Spectral dependencies of magneto-optical Kerr effect (Kerr rotation and Kerr ellipticity) in polar configuration are shown in figure 6.4. The samples were measured in the range from 1.1 to 7 eV using the rotating analyzer technique at magnetic field 1 T. However, no signal was measured above 5.5 eV and zero Kerr rotation was observed below 2.4 eV. Therefore, the data are depicted only from 2.4 to 5.5 eV.

The MOKE spectra are in agreement with the previous measurements [23, 40], yet some differences are observed, e.g. around 4.2 eV as the double peak is much wider then usual.

The data from MOKE measurements were used for the calculation of the off-diagonal elements of the permittivity tensor for each material. The real and imaginary parts of the off-diagonal elements are depicted in figure 6.5.

Comparing the measurements the most interesting difference between these measurements and the measurement of $Y_3Fe_5O_{12}$ in [40] is the width of the double peak in the spectrum in spectral range 4 - 4.5 eV. This abnormal width also follows the studies [35, 36] that gallium, as a rare-earth element, preferably substitutes Fe^{3+} ion at the tetrahedral site. Gallium has a significant effect on the lattice constant as the Ga^{3+} ion is smaller than Fe^{3+} ion. It reduces the lattice constant and the whole cell volume and therefore changes the bond lengths between the iron and oxygen ions and the angle of the Fe^{3+}–O^{2-}–Fe^{3+} linkage in which the Fe^{3+} ions in octahedral and tetrahedral sublattice are linked antiferromagnetically.[36] The

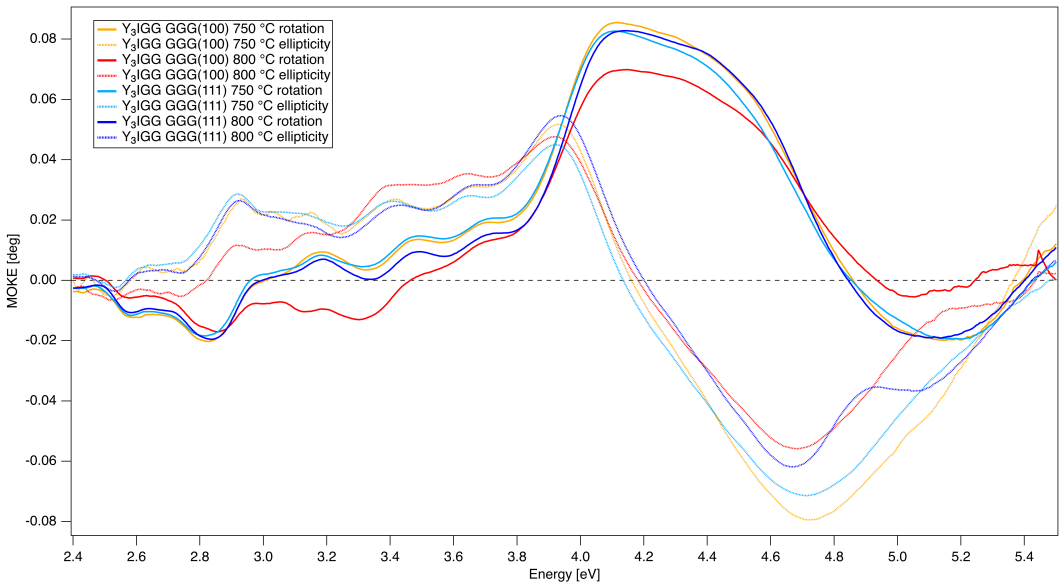

Figure 6.4: Spectral dependencies of MOKE of $Y_3Fe_4Ga_1O_{12}$ on GGG substrates with different orientations.

band lengths get bigger for tetrahedral and smaller for octahedral sublattices with an increasing amount of Ga in the material.[36] It hence causes the transformation of the crystalline field in which the Fe^{3+} is located. According to Lehmann et al. [41] O^{2-}–Fe^{3+} charge transfer transitions occur at a higher energy for the tetrahedral site and at lower energy for the octahedral site. Therefore, the wider double peak points to the fact that gallium substitutes tetrahedral site and decreases the strength of the superexchange interaction and hence lowers the contribution of the octahedral sublattice.

Another difference is that the whole spectrum from 2.4 to 3.8 eV is inclined and shifted towards the upside. It might be because Ga in the tetrahedral site can suppress some of the O^{2-}–Fe^{3+} transitions which can lead to the change of concentration of Fe^{2+} and Fe^{4+} ions that has a great impact on optical and magneto-optical properties.

When comparing the samples, optical and magneto-optical spectra from samples with substrate orientation (100) are slightly different. In the area from 2.8 to 3.8 eV, the spectra have lower amplitude and have slightly different spectral dependencies. In this area, there are several Fe^{3+}–Fe^{3+} electron transitions from octahedral to tetrahedral sublattice. The explanation is that the orientation of the substrate must affect the occupation of individual sublattices by iron ions leading to smaller MO effect at any (annealing) temperature.

The spectra vary also at higher energies but only in the amplitude of the effect. Lower amplitude means lower magnetic moment which means lower saturation magnetization. This leads to a conclusion that in the material with substrate orientation (100), there is a lower concentration of the iron ions or iron with different valence (lower quality of the sample in terms of crystallization) and therefore, the different stoichiometry of the material.

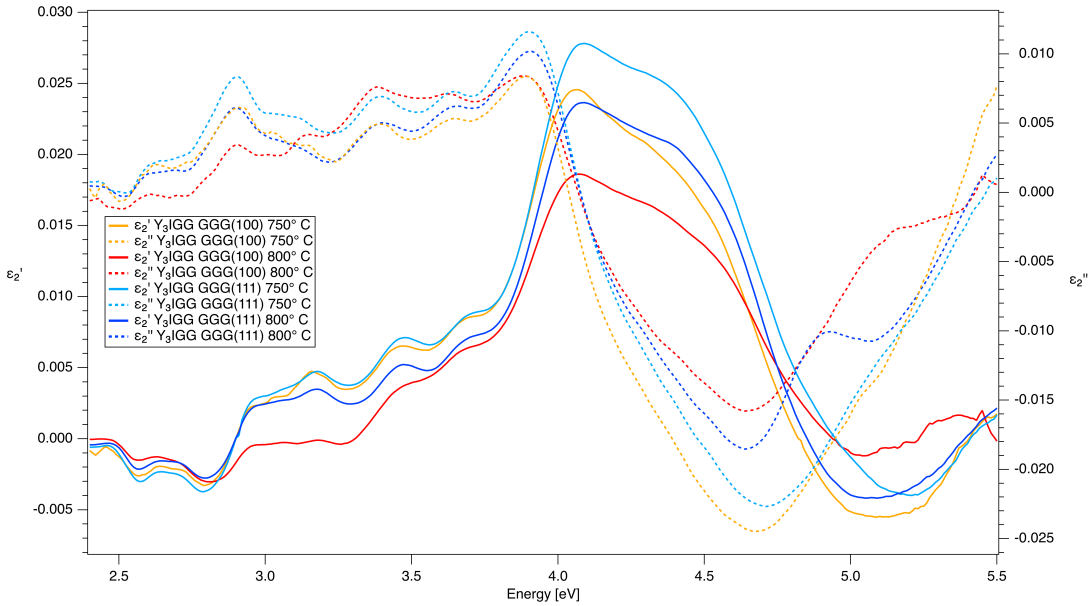

Figure 6.5: Spectral dependencies of the off-diagonal elements of the permittivity tensors of $Y_3Fe_4Ga_1O_{12}$ on GGG substrates with different orientations.

7. $Nd_xBi_{3-x}Fe_4Ga_1O_{12}$ on $Gd_3Ga_5O_{12}$

7.1 Preparation

Another group of garnet thin films was made for the purpose of this study. Bismuth doped neodymium-iron gallium garnets $Nd_xBi_{3-x}Fe_4Ga_1O_{12}$ with different ratio of Nd and Bi and different annealing temperatures on gadolinium gallium garnet ($Gd_3Ga_5O_{12}$) (GGG) substrate with (100) orientation were made also with MOD method. The concentration of solutions used for the deposition was 4 %. The samples were made by the spin coating technique, in which the rotation velocity of the sample holder was 3000 rpm and the rotation lasted 30 seconds. Afterwards the samples were dried on the hot plate for 10 minutes at 100 °C. The final thin films were made firstly by pre-annealing for 10 minutes at 430 °C and then by annealing in an electric furnace for 3 hours at different temperatures (640 °C, 670 °C, 700 °C, 730 °C). Parameters of prepared samples are listed in the table 7.1.

Table 7.1: $Nd_xBi_{3-x}Fe_4Ga_1O_{12}$

material	substrate orientation	annealing temperature	layer thickness	roughness
$Nd_{0.5}Bi_{2.5}Fe_4Ga_1O_{12}$	100	700 °C	18.21 nm[1]	0.01 nm[1]
		640 °C	~30 nm	-
		670 °C	~30 nm	-
		700 °C	~30 nm	-
$Nd_2Bi_1Fe_4Ga_1O_{12}$	100	700 °C	16.57 nm[1]	4.79 nm[1]
		730 °C	16.59 nm[1]	0.12 nm[1]
		640 °C	~30 nm	-
		670 °C	~30 nm	-
		700 °C	~30 nm	-

7.2 Optical properties

Optical constants together with thickness and roughness of the samples were obtained using spectroscopic ellipsometry in a range of angles between 50°and 60° with a step of 5° from ~15 nm thick samples. Because the samples were translucent, the backside of the substrate had to be roughened using a diamond pen and a grinder to avoid backside reflection. Measured data were firstly fitted with a mathematical B-spline model and then parameterized using a combination of 6 Lorentz and Cody-Lorentz oscillators. Oscillators for one chosen sample are depicted in figure 7.1. The result of the fit is shown in figure 7.2. The final optical constants are depicted in figure 7.3.

[1] values from ellipsometry measurements

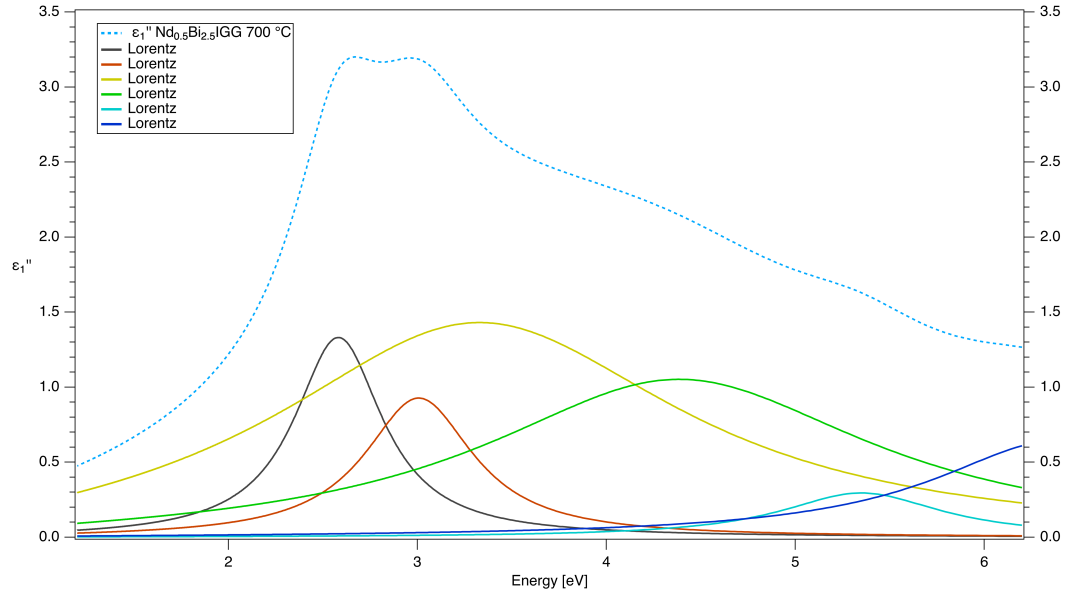

Figure 7.1: Oscillators used for the characterization of sample $Nd_{0.5}Bi_{2.5}Fe_4Ga_1O_{12}$ on GGG(100) substrate (annealing temperature 700 °C).

One can see that the shape of optical constants of $Nd_2Bi_1Fe_4Ga_1O_{12}$ is similar to optical constants of other (bismuth-doped) iron garnets.[23, 42, 43] The sample with higher amount of bismuth has the dependence notably different. Its absorption edge is clearly shifted more into the infrared region and it increases much sooner than the absorption of the other samples. This happens due to the amount of bismuth in the material as it is not observable in less-bismuth-doped samples. In general, bismuth causes higher absorption in the visible spectrum and has a significant impact on magneto-optical properties.[23, 43]

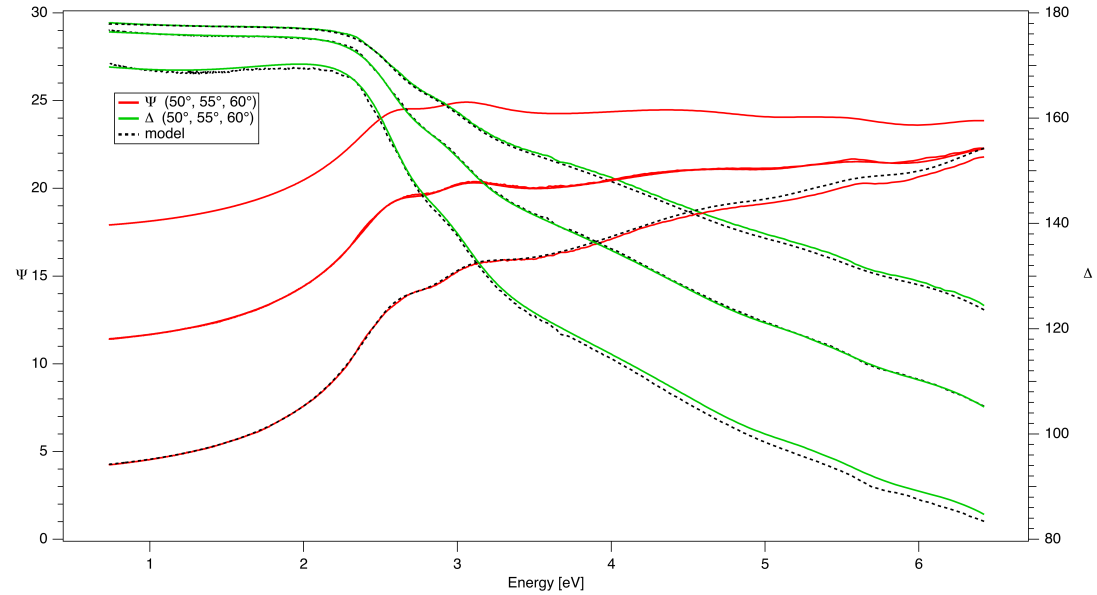

Figure 7.2: Fit of the optical constants Ψ and Δ of the sample $Nd_{0.5}Bi_{2.5}Fe_4Ga_1O_{12}$ on GGG(100) substrate (annealing temperature 700 °C).

The most significant part of the spectrum is the double peak in the range of

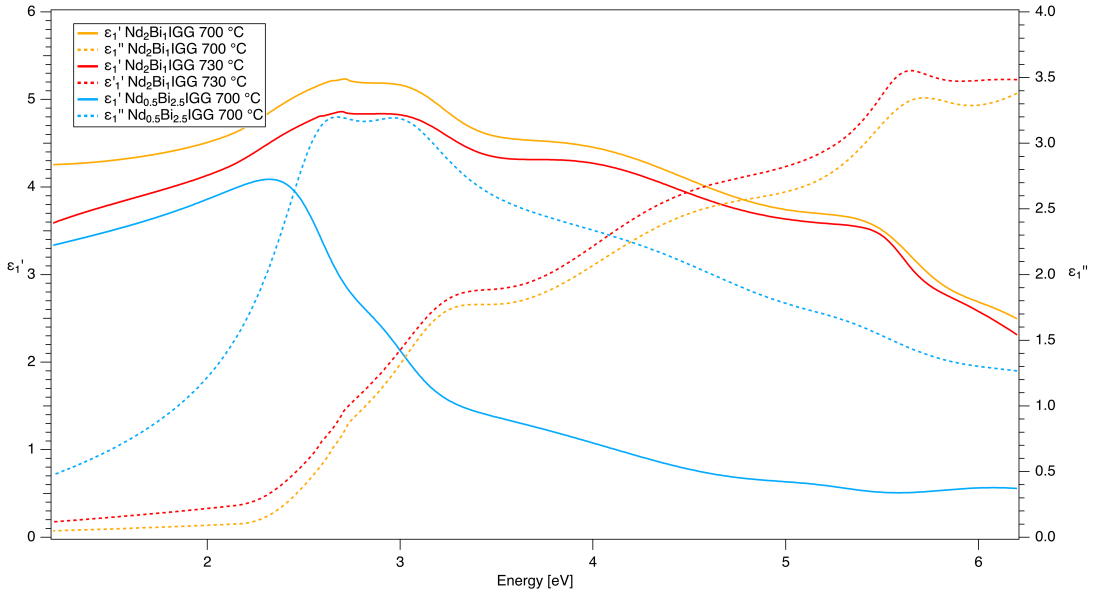

Figure 7.3: Spectral dependencies of the diagonal elements of the permittivity tensors of $Nd_xBi_{3-x}Fe_4Ga_1O_{12}$ on GGG(100) substrates.

energies 2.5 - 3.1 eV for highly bismuth-doped sample. Its origin comes from the contribution of bismuth as it is not visible in non-bismuth-doped garnets and less visible in less-bismuth-doped garnets. According to [42], the mechanism by which bismuth is enhancing the band is not so easy to unravel, hence it most probably comes from the charge transfer transition between Bi^{3+} and Fe^{3+}.

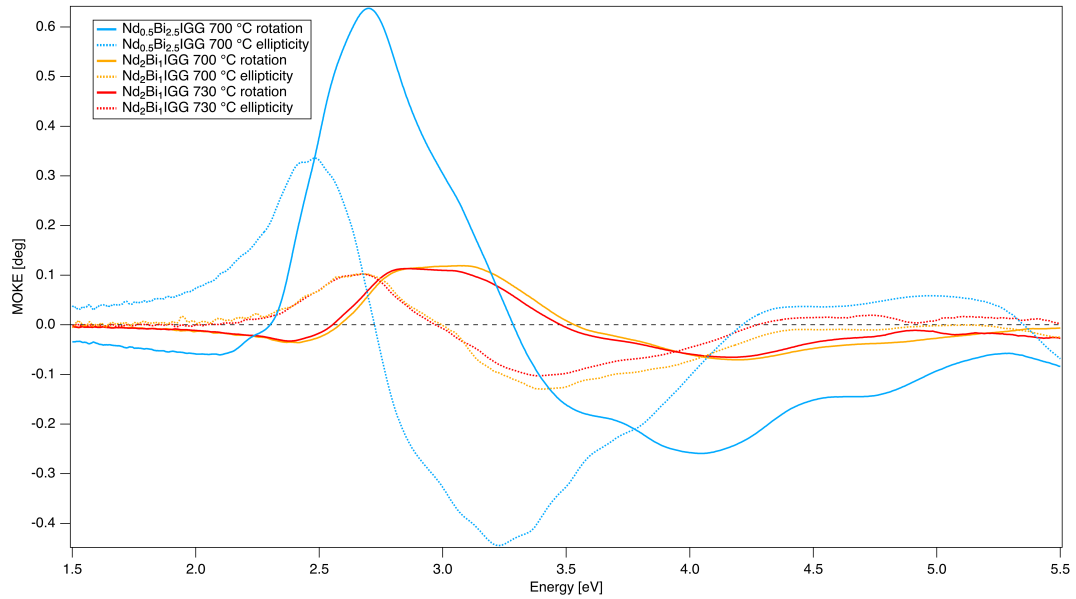

Figure 7.4: Spectral dependencies of MOKE of $Nd_xBi_{3-x}Fe_4Ga_1O_{12}$ on GGG(100) substrates.

7.3 Magneto-optical properties

Magneto-optical Kerr effect spectra for polar configuration are depicted in figures 7.4, 7.5. Experimental data were obtained using the rotating analyzer technique while the samples were in the external magnetic field of 1 T. The measurements were performed using light in the range 1.1 - 7 eV. Due to the lack of the signal below 1.2 and above 6 eV, data are shown only in the range from 1.5 to 5.5 eV.

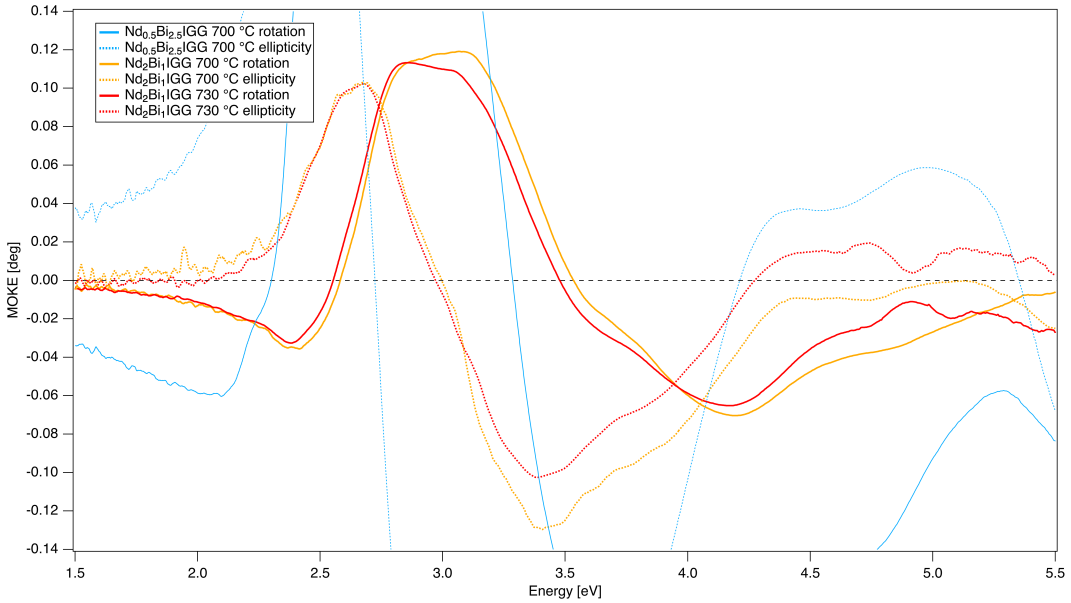

Figure 7.5: The zoom of figure 7.4.

It is clear from the graph that bismuth significantly increases the magneto-optical response of the material. Measured spectra are similar to spectra measured on other iron garnets.[23, 43, 44] In the figure 7.4 one can observe rotation maxima around 2.7, 3.4 and 4 eV and MOKE ellipticity maxima near 3.3 eV, which are characteristic for bismuth doped iron garnets. [23, 45] The less-bismuth-doped samples has also this shape but the effect of bismuth is less visible. The interesting part of the graph 7.6 is the region with the two real parts of the offdiagonal maxima at 2.7 and 3.2 eV in figure 7.5. These maxima are attributed to the O^{2-}–Fe^{3+} charge transfer transitions, which, according to Lehmann et al. [41], occur at a higher energy for the tetrahedral site and at lower energy for the octahedral site. Therefore the different amplitude ratio of the maxima of the two less-bismuth-doped samples indicate that for different temperatures there are different strengths of the superexchange interactions and hence different contribution of individual sublattices. It might be because of the presence gallium in the material. When annealing the sample at a higher temperature, gallium has more energy and therefore it can substitute more easily to the octahedral site. This might outcome in a relatively bigger contribution of the octahedral site to the MO effect.

The data from MOKE and ellipticity measurements were used for the calculation of the off-diagonal elements of the permittivity tensors for these samples. These elements are depicted in figures 7.6 and 7.7.

Faraday hysteresis loops were measured mostly on the ~30 nm thick samples. They were measured at the wavelength of 520 nm. Hysteresis loops of the less-bismuth-doped samples are depicted in the figure 7.8. One can see that

the Faraday rotation in saturation is getting larger with increasing annealing temperature. The same increase can be observed in the case of the coercive field. The coercivity of the sample with annealing temperature 640 °C is almost zero. It might be because at lower temperature in the furnace final crystallization of the sample does not have to be fully completed and hence the sample may be of small magnetocrystalline anisotropy. A higher concentration of Nd and Bi in the sample can serve as another explanation. Due to the higher concentration of bismuth in the material, larger MO effect can be observed as bismuth significantly magnifies the effect via large spin orbit coupling. Additionally, neodymium causes a distortion of the dodecahedral sublattice [46] and therefore the neodymium site can be more strained. It also interacts by ferromagnetic coupling with the total magnetic moment of iron that leads to the modification of the magnetization of the material.

Faraday hysteresis loops of the second set of samples are shown in the figure 7.9. Here, in contrast with the figure 7.8, the measured data are much smoother as the effect is several times larger. The data here do not follow the trends of the increasing Faraday rotation and coercivity with increasing annealing temperature. The explanation is as follows. At higher temperature, bismuth ion has higher thermal kinetics as it responds to temperature more than other components. Bismuth then tries to, at least partially, avoid substitution to dodecahedral site. It tries to replace iron ions in either tetrahedral or octahedral site. This has the effect of lower Faraday rotation in saturation as can be seen on the green curve on figure 7.9.

In the figure 7.10 one can see the Faraday rotation in saturation magnetization and coercive field plotted against the annealing temperature. The "sweet spot" in coercivity and Faraday rotation occurs for the more-bismuth-doped sample in range of temperatures 670 - 700 °C, where the thermal kinetics of bismuth is just right to fully substitute to dodecahedral sublattice. From this measurements one can determine the best deposition conditions when preparing similar types of samples.

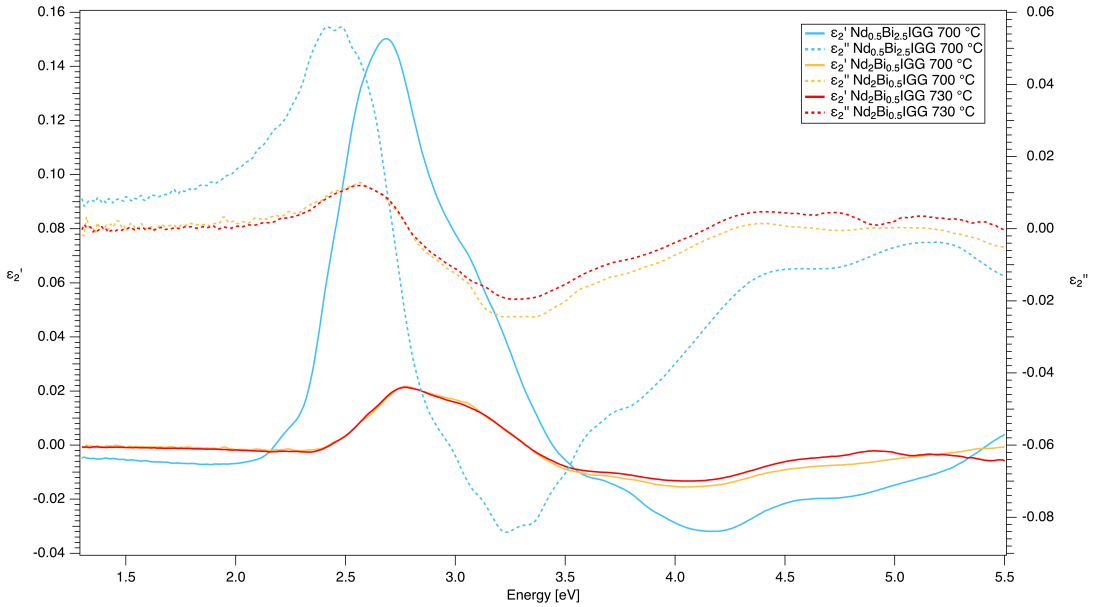

Figure 7.6: Spectral dependencies of the off-diagonal elements of the permittivity tensors of $Nd_xBi_{3-x}Fe_4Ga_1O_{12}$ on GGG (100) substrates.

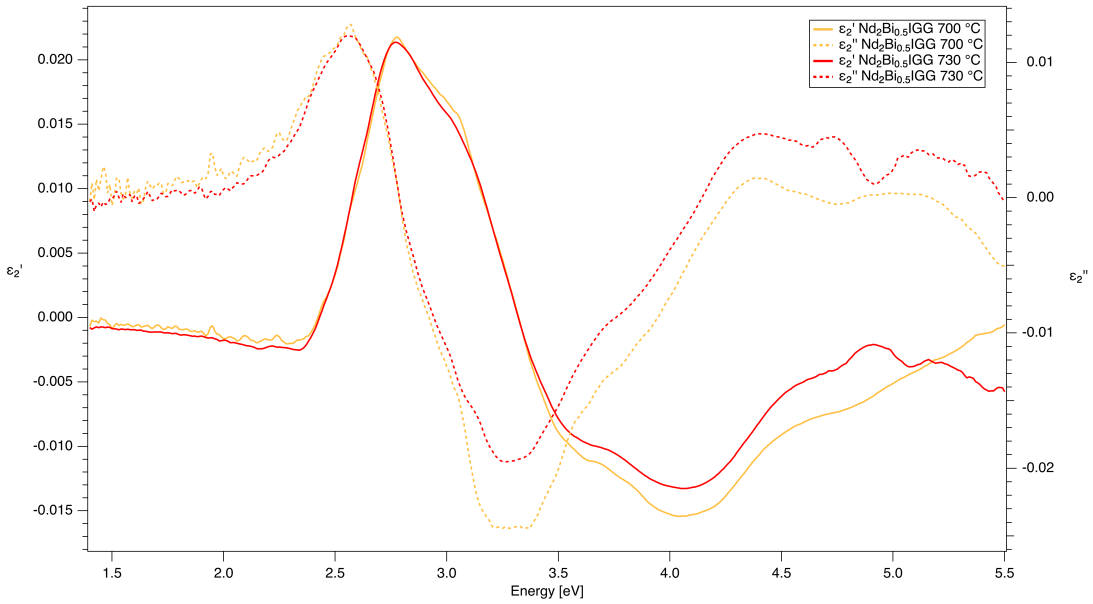

Figure 7.7: Spectral dependencies of the off-diagonal elements of the permittivity tensors of $Nd_2Bi_1Fe_4Ga_1O_{12}$ on GGG (100) substrates (the zoom of figure 7.6).

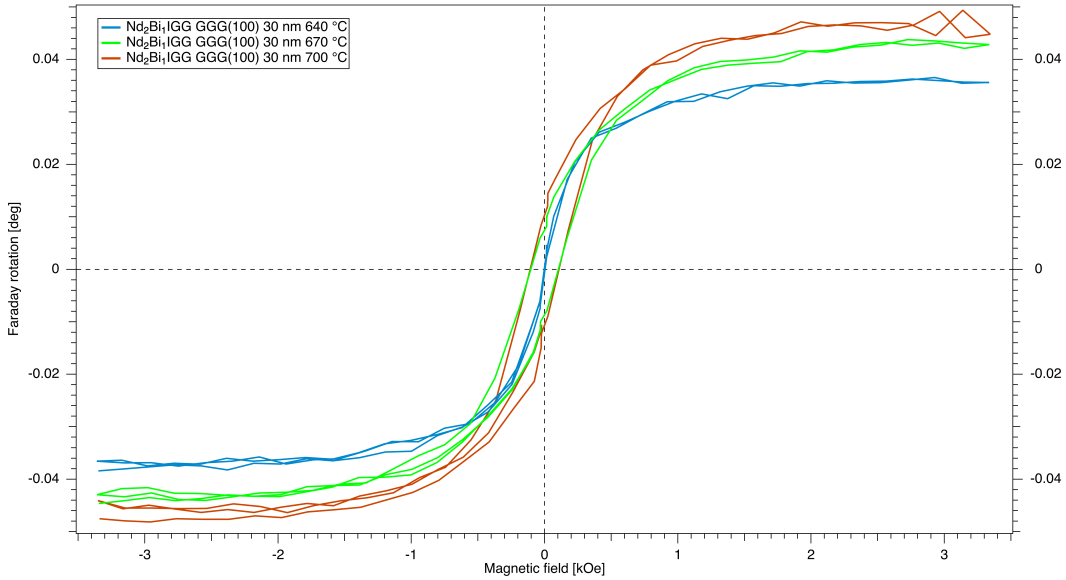

Figure 7.8: Faraday hysteresis loops of the $Nd_2Bi_1Fe_4Ga_1O_{12}$ on GGG(100) substrates.

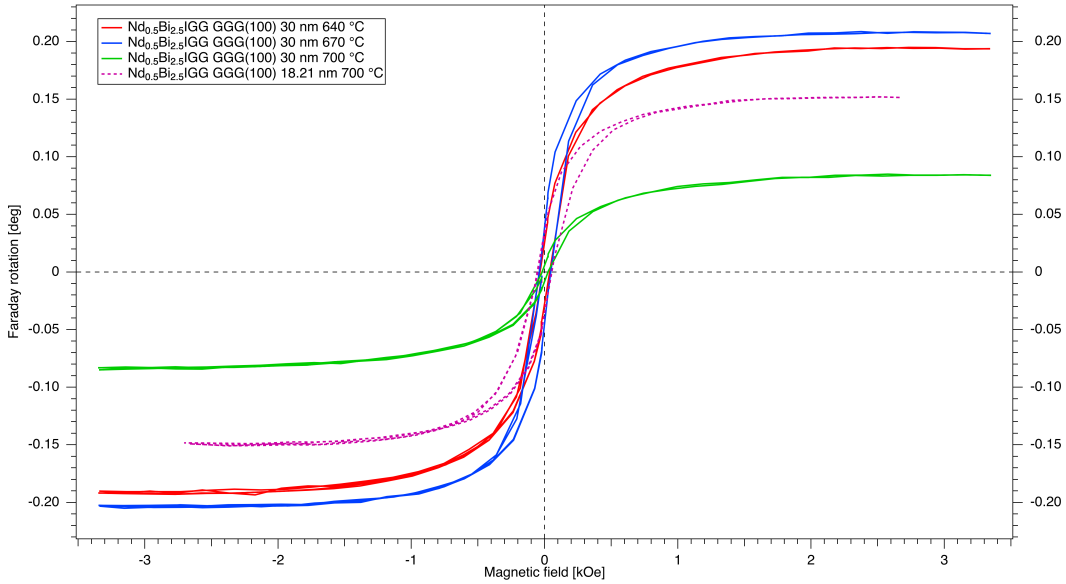

Figure 7.9: Faraday hysteresis loops of the $Nd_{0.5}Bi_{2.5}Fe_4Ga_1O_{12}$ on GGG(100) substrates.

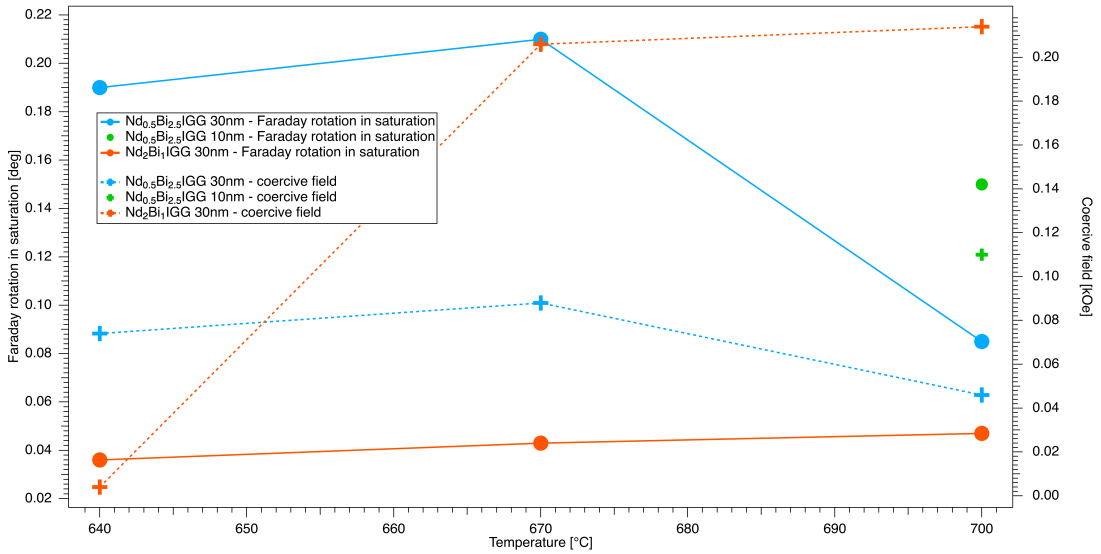

Figure 7.10: Faraday rotation in saturation magnetization and coercive field vs. annealing temperature for samples $Nd_xBi_{3-x}Fe_4Ga_1O_{12}$ on GGG(100) substrates.

Conclusion

In this work, optical and MO methods were used to get an insight into the electronic structure of the studied samples, which were ultra-thin films of iron garnets.

$Y_3Fe_4Ga_1O_{12}$

Two sets of samples were prepared using metal-organic decomposition method with annealing temperatures 750 °C and 800 °C with different orientations of the GGG substrate, (100) and (111). Their optical and magneto-optical properties were studied in spectral region 1.1 - 7 eV. The results showed a slight difference between the films on different substrate orientations and with different annealing temperatures. From the MOKE and ellipsometry measurement, off-diagonal elements of the permittivity tensor were calculated. The spectra show that the substrate orientation affects the occupation of individual sublattices by iron ions and also affect the stoichiometry of the material leading to a lower magneto-optical effect at any annealing temperature. From this point of view, GGG with orientation (111) seems to be the most suitable one.

$Nd_xBi_{3-x}Fe_4Ga_1O_{12}$

Two sets of samples with different compositions, annealing temperatures and thicknesses were prepared with MOD method. Their optical and magneto-optical properties were also studied in spectral region 1.1 - 7 eV. On the thinner samples, MOKE measurements were performed. In the first case, they confirmed that the concentration of bismuth in the material significantly increases MO response. MOKE measurements show that different annealing temperatures might influence the concentration of Ga at individual sublattices. Computed off-diagonal elements of permittivity tensor confirm that idea.

Faraday hysteresis loops were measured on the thicker (30 nm) samples. Almost zero coercive fields were observed on less-bismuth-doped samples with annealing temperature 670 °C. This might be because of the incomplete crystallization of the sample. Another explanation is a higher concentration of Nd and Bi in the samples with higher annealing temperatures. However, more-bismuth-substituted samples have different temperature dependence. It might be because with increasing annealing temperature, bismuth has more kinetic energy during the process. It then does not fully substitute to the dodecahedral site as it tries to substitute iron ions in either tetrahedral or octahedral site. It turns out that for the highest MO effect in saturation magnetization and the largest coercive field, the annealing temperatures for more-bismuth-doped samples should be between 670 - 700 °C.

In conclusion, both groups of materials have the expected properties of ferrimagnetic garnets. Both groups, even though their thicknesses are very small, show large MO effect, especially the more-bismuth-doped sample $Nd_{0.5}Bi_{2.5}Fe_4Ga_1O_{12}$ as it has the maximum Kerr rotation about 0.6 degrees. From the performed

measurements, one can assume that metal-organic decomposition method of preparation of samples fabricates samples of very high quality.

Bibliography

[1] M. Mitchell Waldrop. "The chips are down for Moore's law". In: *Nature* 530.7589 (2016), pp. 144–147. DOI: 10.1038/530144a.

[2] R. W. Keyes. "Miniaturization of electronics and its limits". In: *IBM Journal of Research and Development* 44.1.2 (2000), pp. 84–88. DOI: 10.1147/rd.441.0084.

[3] Mark Hopkinson. *With silicon pushed to its limits, what will power the next electronics revolution?* Aug. 2015. URL: https://phys.org/news/2015-08-silicon-limits-power-electronics-revolution.html.

[4] *The Application of Spintronics*. URL: https://www.ibm.com/ibm/history/ibm100/us/en/icons/spintronics/.

[5] Jifeng Liu et al. "Ge-on-Si laser operating at room temperature". In: *Optics Letters* 35.5 (2010), p. 679. DOI: 10.1364/ol.35.000679.

[6] Chen Sun et al. "Single-chip microprocessor that communicates directly using light". In: *Nature* 528.7583 (2015), pp. 534–538. DOI: 10.1038/nature16454.

[7] Nsf. *A Multi-Component Photonic Integrated Circuit*. Aug. 2016. URL: https://www.eurekalert.org/multimedia/pub/121558.php.

[8] Taichi Goto et al. "A nonreciprocal racetrack resonator based on vacuum-annealed magnetooptical cerium-substituted yttrium iron garnet". In: *Optics Express* 22.16 (2014), p. 19047. DOI: 10.1364/oe.22.019047.

[9] Mehmet C. Onbasli et al. "Integration of bulk-quality thin film magneto-optical cerium-doped yttrium iron garnet on silicon nitride photonic substrates". In: *Optics Express* 22.21 (2014), p. 25183. DOI: 10.1364/oe.22.025183.

[10] Lei Bi et al. "On-chip optical isolation in monolithically integrated non-reciprocal optical resonators". In: *Nature Photonics* 5.12 (2011), pp. 758–762. DOI: 10.1038/nphoton.2011.270.

[11] F. Forlini and N. Minnaja. "The coercive force of a ferrimagnetic garnet near its compensation temperature". In: *IEEE Transactions on Magnetics* 2.4 (Dec. 1966), pp. 770–770. DOI: 10.1109/TMAG.1966.1065984.

[12] Miroslav Nývlt. *Optical interactions in ultrathin magnetic film structures*. Charles University, Prague: PhD thesis, Aug. 1996.

[13] Max Born and Emil Wolf. *Principles of optics : electromagnetic theory of propagation, interference and diffraction of light*. Oxford: Pergamon Press, 1980. ISBN: 9780080264820.

[14] Carlo Andrea Gonano, Riccardo Enrico Zich, and Marco Mussetta. "Definition For Polarization P And Magnetization M Fully Consistent With Maxwells Equations". In: *Progress In Electromagnetics Research B* 64 (2015), pp. 83–101. DOI: 10.2528/pierb15100606.

[15] Zachary R. Nunn et al. "Control of the noncollinear interlayer exchange coupling". In: *Science Advances* 6.48 (2020). DOI: 10.1126/sciadv.abd8861.

[16] F. Eskandari et al. “Magnetization and anisotropy of cobalt ferrite thin films”. In: *Physical Review Materials* 1.7 (2017). DOI: 10.1103/physrevmaterials.1.074413.

[17] Svatopluk Krupička. *Fyzika feritů a příbuzných magnetických kysličníků: vysokoškolská učebnice*. Academia, 1969.

[18] Nicola Ann Spaldin. *Magnetic materials fundamentals and device applications*. Cambridge: Cambridge University Press, 2003.

[19] J. M. D. Coey. *MAGNETISM AND MAGNETIC MATERIALS*. Cambridge: Cambridge University Press, 2009.

[20] Lukáš Beran. *Optical and magneto-optical studies of ferrimagnetic garnets for photonic and spintronic applications*. Charles University, Prague: PhD thesis, 2020.

[21] T Kuschel et al. “Vectorial magnetometry using magnetooptic Kerr effect including first- and second-order contributions for thin ferromagnetic films”. In: *Journal of Physics D: Applied Physics* 44.26 (June 2011), p. 265003. DOI: 10.1088/0022-3727/44/26/265003.

[22] Štefan Višňovský. *Optics in magnetic multilayers and nanostructures*. Boca Raton: CRC Taylor & Francis, Mar. 2006. ISBN: 9780849336867.

[23] S. Wittekoek et al. “Magneto-optic spectra and the dielectric tensor elements of bismuth-substituted iron garnets at photon energies between 2.2-5.2 eV”. In: *Physical Review B (Solid State)* 12.7 (Oct. 1975), pp. 2777–2788. DOI: 10.1103/PhysRevB.12.2777.

[24] G. F. Dionne. *Magnetic oxides*. New York: Springer, 2009. ISBN: 978-1-4419-0054-8.

[25] Lukáš Flajšman. *Vectorial Kerr magnetometry*. Brno University of Technology, Brno: master thesis, 2015.

[26] Justin Peatross and Michael Ware. *Physics of light and optics*. Brigham Young University, Department of Physics, 2015.

[27] Harland G. Tompkins and James N. Hilfiker. *Spectroscopic ellipsometry: practical application to thin film characterization*. Momentum press, 2016.

[28] John Arthur Woolam Inc. *CompleteEASE Data Analysis Manual*. Version 3.65. 2008.

[29] T. Okuda et al. “Magnetic properties of $Bi_3Fe_5O_{12}$ garnet”. In: *Journal of Applied Physics* 67.9 (1990), pp. 4944–4946. DOI: 10.1063/1.344740. eprint: https://doi.org/10.1063/1.344740. URL: https://doi.org/10.1063/1.344740.

[30] Oswaldo Alves, Célia Ronconi, and André Galembeck. “Metallo-organic decomposition: A chemical approach to thin film deposition”. In: *Química Nova* 25 (Feb. 2002), pp. 69–77.

[31] Takayuki Ishibashi et al. “Characterization of epitaxial $(Y,Bi)_3(Fe,Ga)_5O_{12}$ thin films grown by metal-organic decomposition method”. In: *Journal of Applied Physics* 97 (Jan. 2005). DOI: 10.1063/1.1827339.

[32] J. W. Weber et al. “B-spline parametrization of the dielectric function applied to spectroscopic ellipsometry on amorphous carbon”. In: *Journal of Applied Physics* 106.12 (2009), p. 123503. DOI: 10.1063/1.3257237.

[33] Joel Mohrmann et al. “Application of a B-spline model dielectric function to infrared spectroscopic ellipsometry data analysis”. In: *Journal of Vacuum Science & Technology B* 38.1 (2020), p. 014001. DOI: 10.1116/1.5126110.

[34] G. B. Scott and J. L. Page. “The absorption spectra of Y3Fe5O12 and Y3Ga5O12:Fe3+ to 5.5 eV”. In: *Physica Status Solidi (b)* 79.1 (1977), pp. 203–213. DOI: 10.1002/pssb.2220790121.

[35] S. Geller et al. “Gallium-Substituted Yttrium Iron Garnet”. In: *Physical Review* 148.2 (1966), pp. 522–524. DOI: 10.1103/physrev.148.522.

[36] Khozima Hamasha et al. “Structural and Magnetic Studies of Ga-doped Yttrium Iron Garnet”. In: *Journal of Wuhan University of Technology-Mater. Sci. Ed.* 36.1 (2021), pp. 13–21. DOI: 10.1007/s11595-021-2372-3.

[37] Eva Jakubisova-Liskova et al. “Optical spectroscopy of sputtered nanometer-thick yttrium iron garnet films”. In: *Journal of Applied Physics* 117.17 (2015). DOI: 10.1063/1.4906526.

[38] G. B. Scott et al. “Magnetic circular dichroism and faraday rotation spectra ofy3fe5o12”. In: *Physical Review B* 12.7 (1975), pp. 2562–2571. DOI: 10.1103/physrevb.12.2562.

[39] A. K. Zvezdin. *Modern magnetooptics and magnetooptical materials*. Bristol Philadelphia, Pa: Institute of Physics Pub, 1997. ISBN: 075030362X.

[40] Š. Višňovský et al. “Polar Kerr rotation spectra in yttrium iron garnet and lithium ferrite: A comparative study”. In: *Applied Physics* 18.3 (1979), pp. 243–247. DOI: 10.1007/bf00885509.

[41] Gerhard Lehmann. “Ligand Field and Charge Transfer Spectra of Fe(III)—O Complexes”. In: *Zeitschrift für Physikalische Chemie* 72.4.6 (1970), pp. 279–297. DOI: 10.1524/zpch.1970.72.4.6.279.

[42] D.E. Lacklison, G.B. Scott, and J.L. Page. “Absorption spectra of Bi3+ and Fe3+ in Y3Ga5O12”. In: *Solid State Communications* 14.9 (1974), pp. 861–863. DOI: 10.1016/0038-1098(74)90151-3.

[43] Eva Jesenska et al. “Optical and magneto-optical properties of Bi substituted yttrium iron garnets prepared by metal organic decomposition”. In: *Optical Materials Express* 6.6 (2016), p. 1986. DOI: 10.1364/ome.6.001986.

[44] M. Veis et al. “Polar and longitudinal magneto-optical spectroscopy of bismuth substituted yttrium iron garnet films grown by pulsed laser deposition”. In: *Thin Solid Films* 519.22 (2011), pp. 8041–8046. DOI: 10.1016/j.tsf.2011.06.007.

[45] P. Hansen and J.-P. Krumme. “Magnetic and magneto-optical properties of garnet films”. In: *Thin Solid Films* 114.1-2 (1984), pp. 69–107. DOI: 10.1016/0040-6090(84)90337-7.

[46] Takashi Komori et al. “Trineodymium(III) pentairon(III) dodecaoxide, Nd3Fe5O12”. In: *Acta Crystallographica Section E Structure Reports Online* 65.10 (2009), pp. i72–i72. DOI: 10.1107/s1600536809036794.

List of Figures

Acronyms

CCD charge-coupled device. 32

GGG gadolinium gallium garnet ($Gd_3Ga_5O_{12}$). iii, 38, 42, 43, 44, 45, 46, 47, 48, 49, 52, 53, 54, 55, 60, 61

LCP left circular polarization. 12, 24, 27

MCD magnetic circular dichroism. 16

MO magneto-optical. 1, iii, 3, 4, 6, 9, 16, 22, 23, 28, 31, 34, 38, 41, 45, 48, 50, 51, 55, 60

MOD metal-organic decomposition. iii, 30, 38, 42, 47, 55, 56, 60

MOKE magneto-optical Kerr effect. iii, 16, 22, 23, 31, 32, 44, 45, 49, 50, 55, 60

PMA perpendicular magnetic anisotropy. 21

RAM random-access memory. 3

RCP right circular polarization. 12, 24, 27

YIG yttrium-iron garnet ($Y_3Fe_5O_{12}$). 18, 37, 60